OPEN ACCESS



Mapping Dark Matter with Extragalactic Stellar Streams: The Case of Centaurus A

Sarah Pearson^{1,7}, Adrian M. Price-Whelan², David W. Hogg^{1,2,3}, Anil C. Seth⁴, David J. Sand⁵, Jason A. S. Hunt², and Denija Crnojević⁶

² Center for Computational Astrophysics, Flatiron Institute, 162 5th Ave, New York City, NY 10010, USA

³ Max-Planck-Institut für Astronomie, Königstuhl 17, D-69117 Heidelberg, Germany

⁴ Department of Physics and Astronomy, University of Utah, Salt Lake City, UT 84112, USA

⁵ Department of Astronomy and Steward Observatory, University of Arizona, 933 N Cherry Ave, Tucson, AZ 85719, USA

⁶ University of Tampa, 401 West Kennedy Boulevard, Tampa, FL 33606, USA

Received 2022 May 21; revised 2022 October 17; accepted 2022 October 18; published 2022 December 8

Abstract

In the coming decade, thousands of stellar streams will be observed in the halos of external galaxies. What fundamental discoveries will we make about dark matter from these streams? As a first attempt to look at these questions, we model Magellan/Megacam imaging of the Centaurus A (Cen A) disrupting dwarf companion Dwarf 3 (Dw3) and its associated stellar stream, to find out what can be learned about the Cen A dark matter halo. We develop a novel external galaxy stream-fitting technique and generate model stellar streams that reproduce the stream morphology visible in the imaging. We find that there are many viable stream models that fit the data well, with reasonable parameters, provided that Cen A has a halo mass larger than $M_{200} > 4.70 \times 10^{12} M_{\odot}$. There is a second stream in Cen A's halo that is also reproduced within the context of this same dynamical model. However, stream morphology in the imaging alone does not uniquely determine the mass or mass distribution for the Cen A halo. In particular, the stream models with high likelihood show covariances between the inferred Cen A mass distribution, the inferred Dw3 progenitor mass, the Dw3 velocity, and the Dw3 line-of-sight position. We show that these degeneracies can be broken with radial-velocity measurements along the stream, and that a single radial velocity measurement puts a substantial lower limit on the halo mass. These results suggest that targeted radial-velocity measurements will be critical if we want to learn about dark matter from extragalactic stellar streams.

Unified Astronomy Thesaurus concepts: Galaxy dynamics (591); Dark matter (353); Stellar streams (2166); Galaxy structure (622); Galaxy dark matter halos (1880); Galaxy stellar halos (598)

1. Introduction

When a dwarf galaxy is accreted by a larger galaxy, a tidal interaction unfolds that can lead to the formation of stellar streams (e.g., Johnston et al. 1995). The collective velocities and positions of stars in stellar streams can store dynamical information from billions of years of past evolution (e.g., Johnston et al. 2001).

From studies in the Milky Way (MW), we know that stellar streams provide information on the Galactic accretion history (e.g., Belokurov et al. 2006; Naidu et al. 2020). Streams in the MW have also been used to constrain the enclosed dark matter distribution of our galaxy (e.g., Koposov et al. 2010; Küpper et al. 2015) and to investigate the shape of the MW's dark matter halo (e.g., Law & Majewski 2010; Vera-Ciro & Helmi 2013; Pearson et al. 2015; Bovy et al. 2016). Additionally, stellar streams trace out orbits of comoving stars close in energy and angular momentum space, which make streams powerful probes of orbit structures in galaxies (i.e., thin streams can only exist on regular or near-resonant orbits: Price-Whelan et al. 2016; Yavetz et al. 2021, T. Yavetz et al. 2022, in preparation).

Original content from this work may be used under the terms of the Creative Commons Attribution 4.0 licence. Any further distribution of this work must maintain attribution to the author(s) and the title of the work, journal citation and DOI.

Bonaca & Hogg (2018) showed that stream tracks in the MW hold key information on the local acceleration field and enclosed mass, and that longer streams on more eccentric orbits best constrain the dark matter halo shape. They also show that the joint constraint, from multiple streams, provides more information than the sum of individual stream tracks. In the MW, we can obtain 6D phase-space measurements for individual stars in stellar streams (e.g., Fritz & Kallivayalil 2015; Price-Whelan & Bonaca 2018; Li et al. 2019; Shipp et al. 2019; Li et al. 2022). However, in external galaxies, we cannot directly build on the intuition from Bonaca & Hogg (2018), because we observe streams in projection, where the physical scale of the system depends on the distance to the external galaxy of interest. We often only have access to 2D morphological measurements, but stellar kinematic and distance measurements do exist for some streams (e.g., from GCs (Veljanoski et al. 2014), from surface brightness fluctuations (Toloba et al. 2016a), and from HST observations of the tip of the red-giant branch (Crnojević et al. 2019)).

Individual stellar streams from accreted dwarf galaxies have been observed around both massive external galaxies (e.g., Shang et al. 1998; Martin et al. 2014; Martinez-Delgado et al. 2021) and around dwarf galaxies (e.g., Martínez-Delgado et al. 2012; Toloba et al. 2016a; Kado-Fong et al. 2018; Carlin et al. 2019; Kado-Fong et al. 2020). We are finally entering an era in astronomy, where we will have access to statistical samples of stellar streams that orbit external galaxies. Ground-based surveys, such as the Vera Rubin Observatory (Rubin; Ivezic et al. 2008), and space telescopes, such as Euclid (Laureijs et al. 2011) and the Nancy Grace Roman Space

⁷ Hubble Fellow.

Telescope (Roman; Spergel et al. 2013), will discover thousands of stellar streams in galaxies out to hundreds of Mpc (e.g., Laine et al. 2018). The astronomical community has prepared for this by developing techniques to automate stellar stream detection in external galaxies (e.g., Pearson & Clark 2021; Pearson et al. 2022), and to automatically classify substructure (e.g., streams versus shells in Hendel et al. 2019).

While stellar streams in external galaxies could provide a fundamental way of mapping dark matter, we still lack theoretical counterparts to interpret stellar stream observations. Fardal et al. (2013) modeled the Giant Southern Stream (GSS) and used Bayesian sampling of N-body simulations to infer M31's mass (see also Fardal et al. 2007, 2009). They took advantage of data from both photometric mapping projects, such as PAndAS (e.g., McConnachie et al. 2009, 2018), and of radial velocities measurements for individual red-giant branch stars in the halo of M31, which were obtained with 8-10 m class telescopes (e.g., Ibata et al. 2004; Gilbert et al. 2009). The best-fit models in Fardal et al. (2013) reproduce both the observed distance and velocity gradients along the stream. But in most external galaxies, we do not have access to such info. van Dokkum et al. (2019) provided an example of a fit to a stream well beyond the Local Group, NGC 5907. While they showed that a match to the stream morphology was possible, they did not explore the stream's constraining power on NGC 5907's halo parameters. It therefore remains largely unexplored what we can learn about external galaxies' dark matter halo properties beyond the Local Group (i.e., mass distributions, dark matter concentrations, and shapes) from their populations of stellar streams.

In this paper, we take the first step toward using extragalactic stellar streams beyond the Local Group to map dark matter. Specifically, we explore what the streams around the elliptical galaxy, Centaurus A (Cen A), located 3.8 Mpc (Harris et al. 2010) from the Milky Way, can teach us about Cen A's dark matter halo. We first develop a stream-modeling technique for streams evolved in external galaxies, and compare model streams to data from the Magellan Clay 6.5 m telescope (Crnojević et al. 2016). This method can be applied to any external galaxy. We find that we can easily reproduce the morphology of the Dw3 stream in an NFW potential motivated by the enclosed mass of globular clusters (GCs) in Cen A (Woodley et al. 2010). We also find that the inferred halo mass of Cen A is degenerate with stream morphology if we do not include any radial velocity measurements of Dw3. When we include a radial velocity, however, the Dw3 stream in Cen A prefers a halo mass of at least $M_{200} > 4.70 \times 10^{12} M_{\odot}$. We demonstrate that radial velocities and distance measurements along the stream can help constrain the dark matter halo mass further, as expected from stream-modeling efforts in the MW.

The paper is organized as follows: In Section 2, we present the data of Cen A. In Section 3, we first present our method for generating model streams in Cen A's potential and our assessment of how well the model streams fit the data. In Section 4, we present the results of our analysis. We discuss our results in Section 5, and we conclude in Section 6.

2. Data

Centaurus A (Cen A or NGC 5128) is located 3.8 Mpc from the Milky Way (Harris et al. 2010), and it is the nearest massive early-type galaxy. The galaxy has been observed extensively at a range of wavelengths (e.g., Graham 1979; Fabbiano et al. 1992;

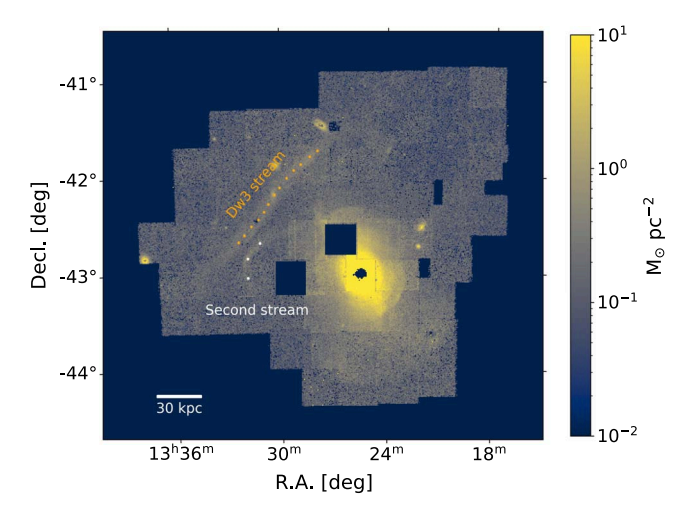


Figure 1. The outer stellar halo density map of RGB stars from Crnojević et al. (2016) obtained with the Magellan Clay 6.5 m telescope calibrated to be in units of $M_{\odot} {\rm pc}^{-2}$. We have overplotted 13 control data stream center points (black) along the Dw3 Stream and three control points (white) along the second stream in Cen A. Note that the actual Cen A galaxy is very small compared to the stellar halo mapped here.

Harris et al. 1999), and it has a pronounced dust ring near its center (Jarrett et al. 2003). Its stellar luminosity has been measured to be $L_K = 1.5 \times 10^{11} L_{\odot}$ (Karachentsev et al. 2002). With a mass-to-light ratio of 0.7 (Silge et al. 2005), this corresponds to a stellar mass of $M_* = 1 \times 10^{11} M_{\odot}$. Several groups have analyzed its diffuse light (Crnojević et al. 2016), globular cluster populations (e.g., Woodley et al. 2010; Hughes et al. 2021; Dumont et al. 2022), satellite populations (Crnojević et al. 2019; Müller et al. 2022), and stellar streams (Crnojević et al. 2016, 2019).

In this paper, we use Magellan/Megacam imaging data (McLeod et al. 2015) from the Magellan Clay 6.5 m telescope at Las Campanas Observatory (Crnojević et al. 2016). We present an RGB stellar density map calibrated to be in units of M_{\odot} pc⁻² in Figure 1. This calibration was done using six HST pointings associated with Dw3 and its stream from Crnojević et al. (2019) combined with Padova isochrones (Bressan et al. 2012) to convert number counts of RGB stars in the fields into stellar mass for a range of metallicities and ages. We averaged the results across the six fields—the derived conversion factor varies by a factor of \sim 2 between fields, and this scatter exceeds the model variations with metallicity and age. We mark the location of the Dwarf 3 stream as well as the "second stream." Throughout this work, we also compare our simulated streams to the measured relative distance along the stream, obtained from modeling the stellar populations in Hubble Space Telescope imaging of the Dw3 stream (Crnojević et al. 2019). We additionally use the radial velocity measurement of the nuclear star cluster in Dw3 from Dumont et al. (2022), as well as the radial velocity measurement of Cen A from Hui et al. (1995) and Hughes et al. (2021). In Table 1, we summarize the observational constraints that we use throughout the paper for Cen A and its streams.

At present day, the Dw3 luminosity is $L_V = 1.5 \times 10^7 L_{\odot}$, excluding its stellar stream. If we assume a mass-to-light ratio of 2, which is appropriate for an old, relatively metal-poor stellar population, this means that the present-day stellar mass is $m_{\rm prog} \sim 3 \times 10^7 M_{\odot}$. In Crnojević et al. (2019), they estimate the original luminosity, using MegaCam data and assuming a distance of 3.88 Mpc, to be $M_V \sim -15$. This corresponds to

Table 1
Observational Data Used for Dwarf 3 Stream Modeling

Parameters	R.A. (deg)	Decl. (deg)	$M_{ m dynamical} \ (M_{\odot})$	L_{K} (L_{\odot})	r ^h (kpc)	distance (Mpc)	vel _{rad} (km s ⁻¹)
Cen A	201.365063	-43.019113	9 × 10	1.5 × 10		$3.8 \pm 0.1^{\circ}$	541 ± 7 ^d
Dwarf 3 ^e	202.585167	-42.191741	_11,a	$1.5 \times 10^{7,11,b}$	2.49 ± 0.17	3.88 ± 0.16	359.6 ± 2.4^{f}
CenA/Dw3 _{relative}	-	-	-	-	-	0.079^{g}	-181.4
Second stream	202.975	-42.85	-	-	-	3.8 ^h	651 ± 13^{i}

Notes.

^a From GCs within 40 kpc (Woodley et al. 2010).

 $L_V = 8 \times 10^7 L_{\odot}$, and thus an initial Dw3 mass of $m_{\rm prog} \sim 1.6 \times 10^8 M_{\odot}$, again assuming a mass-to-light ratio of 2. Throughout the paper, we focus on the stage where the stars are being stripped and ignore any initial dark matter in the progenitor (see a further discussion of this in Sections 3.5 and 4.2).

3. Methods

Our goal is to fit the on-sky track of the Dw3 stream and radial velocity of the Dw3 progenitor to determine what we can learn about the dark matter distribution in Cen A. In this section, we first present the potential we use to simulate Dw3's evolution in the Cen A halo (Section 3.1). We then present the control data points and coordinate system used in the modeling (Section 3.2), followed by a description of our external stream generator (Section 3.3) and our stream-fitting technique (Section 3.4). We finally explain how we run follow-up *N*-body simulations of our best-fit Dw3 stream in Cen A's halo (Section 3.5).

3.1. Potentials

We use a two-component mass model to represent the gravitational field of Cen A, with a Hernquist spherical stellar component with $M_* = 1.5 \times 10^{11}~M_\odot$ and a concentration $b = 4.896 \,\mathrm{kpc}$ (Hernquist 1990). We use a spherical Navarro-Frenk-White (NFW) profile for the dark matter halo (Navarro et al. 1996) implemented in gala (Price-Whelan 2017; Price-Whelan et al. 2020). Throughout this work, the halo mass concentration, c, is set by the mass-concentration relation in Equation (5) in Muñoz-Cuartas et al. (2011). We first explore the Dw3 stream's evolution in a fixed potential (see black solid line in Figure 2) motivated by the enclosed mass estimates from GC kinematics (Woodley et al. 2010): $M(R < 40 \text{ kpc}) = 9.7 \pm 3.3 \times 10^{11} M_{\odot}$ (see black data point in Figure 2). In this potential, $M_{200} = 9.4 \times 10^{12} M_{\odot}$ and c = 8.05182. We refer to this potential as the fiducial potential. To explore the minimum halo mass of Cen A in which we can reproduce the Dw3 stream, we also vary the potential parameters of Cen A in a mass range of 0.1–1.9 \times $M_{200,fiducial}$ with c updated accordingly from Muñoz-Cuartas et al. (2011) (see the 10 colored lines in Figure 2 and the potential values in Table 2). We also plot the

projected separation of Dw3 and Cen A (79 kpc) as a green vertical line for reference.

3.2. Control Points & Coordinate System

To explore which dark matter halo potentials of Cen A allow us to reproduce the straight stream emerging from Dw3, we need to compare stream models on various orbits to the data. For this purpose, we place 13 control points, x_n , by eye, along the center of the stream (see orange points in Figure 1). We treat these as our data points for delineating the track of the stream on the sky.

We also define two new coordinate systems, which we summarize in Figure 3. The first new coordinate system has longitude and latitude as ϕ_1 and ϕ_2 , respectively, and it is centered on the Cen A stellar distribution and rotated by $\alpha = 47.76^{\circ}$ to roughly align the Dw3 stream with constant latitude. We use the ICRS coordinates of Dw3 and Cen A, respectively, to define this rotated system such that Cen A is at $(\phi_1, \phi_2) = (0, 0)^{\circ}$ and Dw3 is at $\phi_1 = 0^{\circ}$ (see white dashed lines in Figure 3). In this coordinate system, ϕ_1 is the longitude along the stream (and increases in the direction of motion), and ϕ_2 indicates the direction perpendicular to the stream. For the control points, we define error bars of $\sigma_n = 0.01$ degrees in the direction of ϕ_2 for each data point, x_n , in this frame. This error is set by how far we can move each control point while the point still visually appears to be at the stream center. While a change in σ_n can lead to a different exact value of a loglikelihood function, it will not change our assessment of the best fit.

We then define a coordinate system centered on the three-dimensional position of Cen A by translating to the distance to Cen A (3.8 Mpc) such that the *x*-direction of the new Cartesian coordinate system points in the direction of the Milky Way's center. In this coordinate system, the projected distance between Cen A and Dw3 is fixed to 79 kpc. The other two directions (for *y* and *z*) are shown in Figure 3 (see red arrows). We use this coordinate system to transform stream models generated in the Cen A halo back to the (ϕ_1, ϕ_2) observed sky coordinates in order to evaluate the fits (see Section 3.4).

^b Karachentsev et al. (2002).

^c Harris et al. (2010).

^d From planetary nebulae (Hui et al. 1995).

^e See also Crnojević et al. (2019).

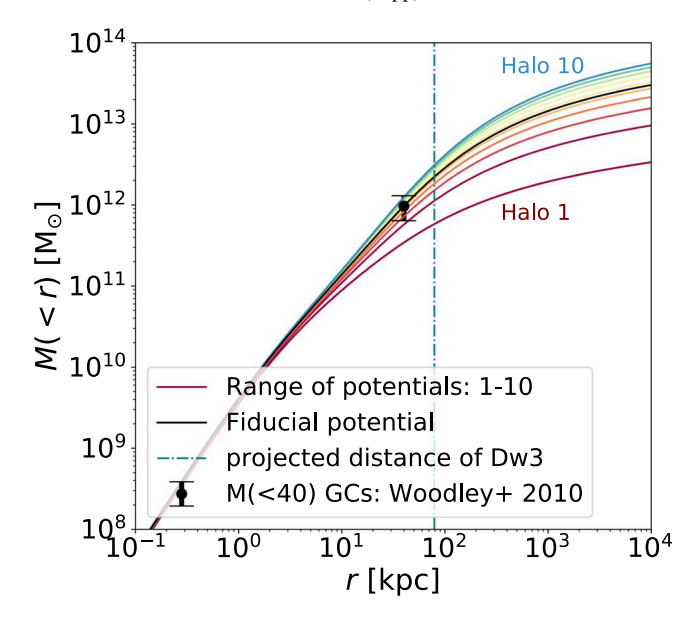
f Dumont et al. (2022).

^g Projected distance (equivalent to 1.22 degrees) assuming a Cen A distance of 3.8 Mpc.

h We place the second stream at 3.8 Mpc, because Crnojević et al. (2016) find that this stream and Cen A are at the same distance.

i Hughes et al. (2022).

⁸ In detail, we define this coordinate frame using the Astropy coordinate transformation system (Astropy Collaboration et al. 2013, 2018), making use of the SkyOffsetFrame.



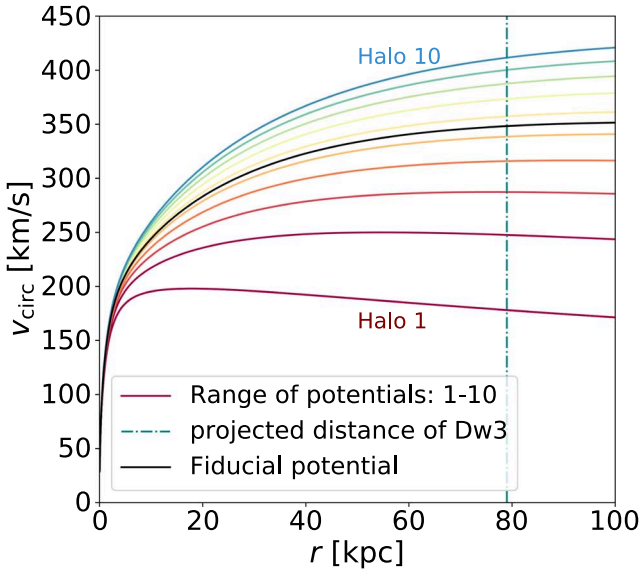


Figure 2. Top: Enclosed mass of the fiducial potential as a function of galactic radius (black solid line). This potential includes a Hernquist stellar component and an NFW dark matter halo component ($M_{200, \mathrm{fiducial}} = 9.4 \times 10^{12}~M_{\odot}$) motivated from GC kinematic estimates within 40 kpc (Woodley et al. 2010; see black data point). The colored lines show a range of potentials with the same Hernquist stellar component, but with varying NFW profiles (colored lines; $M_{200} = 0.94 - 17.86 \times 10^{12}~M_{\odot}$, where red is Halo 1 and blue is Halo 10), which we use throughout the paper (see also Table 2). We use the halo mass vs. halo concentration relation from Muñoz-Cuartas et al. (2011). The vertical teal line shows the projected distance from Dw3 to the center of Cen A. Bottom: Circular velocity as a function of galactic radius for the fiducial potential (black line) as well as the range of potentials (colored lines).

Finally, we transform the simulated streams to the ICRS coordinates, to record the observable radial velocities and distance gradients along the model streams.

3.3. Stream Modeling

To simulate Dw3's stream evolution in Cen A's halo, we generate model streams using the "particle spray" method (Fardal et al. 2015) implemented in gala (Price-Whelan 2017; Price-Whelan et al. 2020). For a given position and velocity of Dw3, we integrate its orbit backward in time over 6 Gyr. From

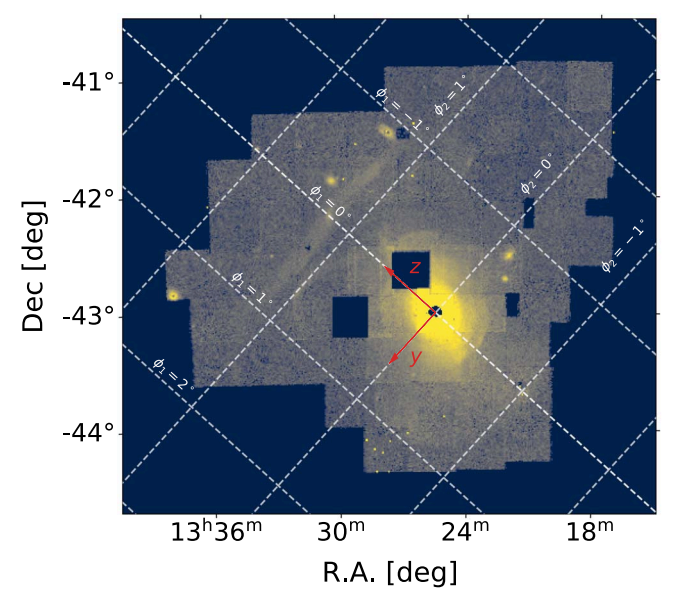


Figure 3. The same data as shown in Figure 1, but here we overplot the two other coordinate systems used in the paper: the galactic coordinate system (x, y, z) used for stream modeling (red), as well as the ϕ_1 , ϕ_2 coordinate system that is centered on Cen A and rotated by 47.76 deg, such that Dw3 is located at $\phi_1 = 0$ (white). We use the latter to visualize our mock stream fits throughout the paper.

Table 2 Summary of Potentials

	$M_{200} M_{\odot} \times 10^{12}$	С	$M(R < 40 \text{ kpc})$ $M_{\odot} \times 10^{11}$	$-\ln \mathcal{L}^{a}$
Fiducial	9.4	8.0518	9.7	3.16
Halo 1	0.94	10.0669	3.43	_
Halo 2	2.82	9.0493	5.73	29.85
Halo 3	4.70	8.6118	7.21	7.83
Halo 4	6.58	8.3353	8.35	4.84
Halo 5	8.46	8.1345	9.29	3.50
Halo 6	10.34	7.9777	10.1	2.86
Halo 7	12.22	7.8495	10.8	2.80
Halo 8	14.10	7.7413	11.4	2.22
Halo 9	15.98	7.6479	12.0	1.89
Halo 10	17.86	7.5658	12.5	2.09

Note.

the orbit end point, we integrate the orbit forward while we release two stars from each Lagrange point per Myr, with a spread in position and velocity dispersion set by the progenitor's mass (see Fardal et al. 2015). We include self-gravity of the progenitor, which we model as a Plummer sphere (Plummer 1911) with $m_{\rm Dw3}=10^8\,M_\odot$ and b=2.5 kpc in order to ensure a realistic length of the stream (Gibbons et al. 2014). This progenitor mass produces model streams with widths similar to that of the observed stream. The widths of the streams are left as free parameters in our assessments of the fits to the control data. We do not update the mass of the progenitor throughout its orbit, as this will only slightly affect the dispersion in position and velocity of the released particles (but see how we consider the evolving mass of the progenitor below).

Using the Fardal et al. (2015) mock stream generator enables us to rapidly explore many different Dw3 orbits as compared to

^a See discussion of these values in Section 4.4.

full *N*-body simulations. One major caveat with this method, however, is that, in reality, Dw3 will not strip stars if the tidal radius is larger than the actual radius of Dw3. This is not taken into account when the "particle spray" stream code releases stars in each time step. To ensure that we do not include streams that would not have formed (i.e., if the progenitor is on first infall or orbiting too far from Cen A's center to strip), we also calculate the Jacobi radius, which can be expressed as

$$r_J = R \left(\frac{m_{\text{prog}}}{M(\langle R)} \right)^{1/3},\tag{1}$$

where R is the galactocentric radius at a given time, m_{prog} is the Dw3 progenitor mass, and M(< R) is the enclosed mass of the potential at the current radius of the orbit. The Jacobi radius changes throughout the evolution of a noncircular orbit and with mass loss of the progenitor. From Figure 9 of Crnojević et al. (2016), we know that Dw3's present-day tidal radius is $r_{\rm tidal,Dw3} \sim 3.3 \, \rm kpc$. Therefore, we add an additional postprocessing step to our mock stream generator, where we remove stars that were released with the "particle spray" method while the Jacobi radius for the simulated dwarf was $r_J > 2 \times r_{\rm tidal,observed}$. We refer to this as the "Jacobi radius criterion" throughout the paper. While we do not update the mass of the progenitor in the stream modeling, we do assume that Dw3 decreases in mass from $1 \times 10^8 M_{\odot}$ to $3 \times 10^7 M_{\odot}$ throughout its 6 Gyr of evolution when we calculate the Jacobi radius (see observational motivation for this in Section 2). Note that a cut of $2 \times r_{\text{tidal,observed}}$ is quite conservative and will often lead to stars stripping along the entirety of Dw3's orbit.

3.4. Comparison to Observational Data

To evaluate how well our model stream tracks fit the control data points, we compute the center point of the simulated streams, y_n , evaluated at the location of the control data, x_n , in the (ϕ_1, ϕ_2) coordinate frame in degrees, where the Dw3 stream is horizontal. This allows us to ignore any horizontal error bars. We compute the log-likelihood:

$$\ln \mathcal{L} = -\frac{1}{2} \sum_{n} \frac{(x_n - y_n)^2}{\sigma^2},\tag{2}$$

where x_n are the 13 control data points, y_n are the 13 simulation evaluation points, and $\sigma = 0.01$ deg is the vertical error in the ϕ_2 -direction. We pick a regularly spaced grid of longitude (ϕ_1) values by eye and assume that we know these values perfectly. The density of the stream has some error in the perpendicular (ϕ_2) direction, and we place the control points along the stream's center by eye with a precision that we assume to be $\sigma = 0.01$ deg. The best fit is when the model stream center points, y_n , have the minimum squared deviation from the control data points, x_n (see Equation (2)). Throughout this work, we evaluate $\ln \mathcal{L}$ both before and after we apply our Jacobi radius criterion (see Section 3.3), and we discard model streams that do not cover the extent of the data points by setting $\ln \mathcal{L} = -\inf$ for those cases. The length, width, and surface density of the model streams are left as free parameters throughout this paper (see Erkal et al. 2017, for an alternative approach including these parameters).

3.5. N-body Follow-up

To check whether the Fardal et al. (2015) mock stream generator produces a similar stellar stream under more realistic stripping conditions, we also run follow-up N-body simulations of our best-fit stream models. In particular, we set up Dw3 as a two-component mass model. We again represent the stellar component of Dw3 as a Plummer sphere (Plummer 1911) with a mass of $1 \times 10^8 \,\mathrm{M_\odot}$ and scale radius $b = 2.5 \,\mathrm{kpc}$, but now we also include a Hernquist sphere (Hernquist 1990) to represent the dark matter $(r_s = 5 \text{ kpc}, M_{dm} = 64 \times M_* = 6.4 \times 10^9 M_{\odot})$. We use the galactic dynamics Python package Agama to sample 10⁶ particles from the Plummer stellar profile and 1.6×10^6 particles from the Hernquist dark matter profile. Next, we initialize this dwarf galaxy at the end point of the integration for the best-fit model stream, and then we integrate the dwarf for 6 Gyr within the same fixed fiducial Cen A potential (see black line in Figure 2) using the N-body simulation code GCD+ (Kawata & Gibson 2003).

4. Results

In this section, we present the results of our Dw3 stream analyses. We first fix the Cen A dark matter halo profile, to explore which orbit solutions can reproduce the straight stream emerging from Dw3 (Section 4.1). We follow up our best-fit stream with an *N*-body code (Section 4.2). We then explore the degeneracy between the dark matter halo mass and stream morphology in Section 4.3, and finally we search for the best-fit solution to the Dw3 stream control data while varying Cen A's dark matter potential in Section 4.4. Throughout this section, we assume a distance to Cen A of 3.8 Mpc and a distance to Dw3 of 3.88 Mpc (see Section 5 for the effects of varying Dw3's distance). We also assume an initial stellar mass for the progenitor of $m_{\rm Dw3} = 10^8~M_{\odot}$ and scale radius $b = 2.5~{\rm kpc}$, when we simulate the stream. We summarize the simulation parameters used in this section in Table 3.

4.1. Dw3 Stream Morphology and Orbit in a Fixed Cen A Dark Matter Halo

To explore the Dw3 stream evolved in the fiducial potential of Cen A (see Figure 2, solid black line), we first fix Dw3's position and the relative radial velocity between Dw3 and CenA (see Table 1). Thus, the only free parameters in our initial search for orbits that can reproduce the Dw3 stream are the two other Dw3 velocity components. We evaluate the fits to the data in the rotated and shifted coordinate system where Cen A is located at $(\phi_1, \phi_2) = (0, 0)$ deg, with $v_{\rm rad} = 0$ km s⁻¹. The ϕ_1 -direction is parallel to the stream, and the ϕ_2 -direction is perpendicular to the stream (see Section 3.2).

We set up a grid of velocities with v_{ϕ_1} and v_{ϕ_2} ranging from -800 to 800 km s⁻¹ in steps of 50 km s⁻¹. For each velocity combination on this grid, we initialize a model stream simulation (see Section 3.3), integrate the progenitor for 6 Gyr in steps of 1 Myr (see discussion of integration time in Section 5.2), and evaluate the fit of the simulated stream to the actual data as explained in Section 3.4. For each model stream

Note that abundance matching predicts higher dark matter to baryon ratios for dwarfs at this stellar mass scale (e.g., Behroozi et al. 2010), but because we are interested in the stripping of the stellar component, which happens after the outer parts of the dark matter are gone, we do not explore more massive Dw3 dark matter profiles in this work.

Table 3Summary of Simulation Setup

Parameter	Value	Unit
NFW halo Cen A		
$M_{200, \rm fiducial}$	9.4×10^{12}	M_{\odot}
C ₂₀₀ ,fiducial	8.05182	
Hernquist sphere Cen A	A	
$m_{*, \text{fiducial}}$	1×10^{11}	M_{\odot}
$a_{*,\text{fiducial}}^{\text{a}}$	4.896	kpc
Plummer sphere Dw3		
m_{Dw3}	1×10^{8}	M_{\odot}
$b_{ m Dw3}$	2.5	kpc
Other parameters		
d_{CenA}	3.80	Мрс
d_{Dw3}	3.88	Mpc
$t_{\text{integration}}$	6	Gyr
v_{ϕ_1}, v_{ϕ_2}	-800 to 800	km s
$v_{\rm rad}^{}$	-181.4	km s
r_{J} -cut	2×3.3	kpc

Notes.

and for each velocity combination on the grid, we store the value of $-\ln \mathcal{L}$.

In Figure 4 (left), we clearly see that there is one pocket of orbital solutions that can generate a good fit to the data (see gray box). These solutions all reside in the part of velocity space where the progenitor is moving rapidly parallel to the stream (v_{ϕ_1}) and slowly perpendicular to the stream (v_{ϕ_2}) . We explore all directions of motion of Dw3, but the model streams clearly match the data best for orbits moving in the positive v_{ϕ} -direction. This is due to the "S" shape of the Dw3 stream, with the southern (leading) part of the stream being slightly closer to Cen A's center than the northern (trailing) part. We further discuss the "S" shape later in this section. Note that empty parts of the velocity grid presented in Figure 4 (left) represent failed model streams that did not cover the extent of the control data points during the 6 Gyr of evolution. While we disregard model streams that are shorter than the extent of the control data, the maximal extent of the model stream lengths is a free parameter in our fits (see Section 3.4). Therefore, the model streams are often longer than the actual control data. The exact length of streams is set by a combination of integration time and the complex escape conditions from the progenitor, which can also include dark matter. The debris at the end of streams will often be of lower surface density and might not be observable. See Section 4.2 for a discussion of progenitor escape conditions.

To ensure that we resolve the best-fit solution, we initiate a new, zoomed, velocity grid where v_{ϕ_1} ranges from 300–750 km s⁻¹ in steps of 10 km s⁻¹ and v_{ϕ_2} ranges from 15–125 km s⁻¹ in steps of 2.5 km s⁻¹. We initialize new model streams with these new combinations of orbital parameters, and use the same setup as before. We present the results for these model streams in the upper right panel of Figure 4, where we have included all stars in our assessment of $-\ln \mathcal{L}$. Note that the $-\ln \mathcal{L}$ space is not convex. Thus, classical optimization methods will be

nontrivial in this space, which is why we do a brute-force grid search for the best solution. The gray star indicates the orbit that produced the best fit $(-\ln \mathcal{L} = 3.16 \text{ and } (v_{\phi_1}, v_{\phi_2}) = (460, 50) \text{ km s}^{-1})$. Some of these velocity combinations place Dw3 on orbits that would not lead to tidal stripping, however.

Therefore, in the lower right panel of Figure 4, we evaluate $-\ln \mathcal{L}$ after we apply the Jacobi criterion (see Equation (1) and Section 3.3), in order to ensure more realistic stellar stripping conditions. Note that, for many of the orbits with high v_{ϕ_1} (>590 km s⁻¹), most stars are removed with this cut, and the model streams do not cover the extent of the data (see blank space). We find that the best-fit solution is the same as before the Jacobi cut. The Jacobi radius for the progenitor on this orbit remains smaller than two times the observed tidal radius for the duration of the 6 Gyr. Hence, no stars are removed in the Jacobi radius post-processing step. There are several orbits in this fiducial potential that produce good fits (see dark colors), and the Dw3 stream is easily reproduced for high values of v_{ϕ_1} and low values of v_{ϕ_2} . We summarize the parameters of our best fit in the fiducial halo in Table 4.

In Figure 5, we visualize this best-fit model stream from Figure 4. We show the model stream overplotted on the actual image data of Cen A in ICRS coordinates colored by the radial velocity of the stream in Cen A's rest frame (upper left) and the distance gradient along the stream with respect to Cen A (upper right). Most of the stream is moving toward us (with radial velocities relative to Cen A ranging from $v_{\rm rad} = -116.0$ for the most northern control data point to -244.5 km s^{-1} for the most southern control data point). The distance gradient along the stream ranges from 100.6 kpc with respect to Cen A for the most southern control data point to 55.4 kpc for the most northern control data point. We also visualize the best fit in (ϕ_1, ϕ_2) space (lower left), where the stream is moving toward positive ϕ_1 (see arrow). Note here the pronounced "S" shape of both the model stream and the control data, which helped constrain the direction of motion (i.e., the leading arm is the part of the stream that is closer to Cen A's center). We show the evolution of the galactocentric radius in time for the progenitor's orbit in the lower right panel (t = 0 at present day).

For this fit, Dw3 has completed two pericenter passes in 6 Gyr and is approaching pericenter at present day (see vertical lines in the lower right panel). Note the difference between the Jacobi radius at the first $(r_J = 3.42 \text{ kpc})$ versus second $(r_J$ = 2.97 kpc) pericenter. This is due to the mass loss of the progenitor included in our r_I calculation (see Section 3.3). Interestingly, for most of the best-fit solutions, Dw3 is close to pericenter at present day. The progenitor moves most rapidly at pericenter. The fact that the best-fit stream models are mostly at pericenter at present day is likely because the stream needs to move fast in the ϕ_1 -direction to be so straight while remaining bound to Cen A. Note also that the observed blueshifted lineof-sight velocity of Dw3 with respect to Cen A ($v_r = -181.4$ km/s reported by Dumont et al. 2022) is consistent with the corotating line-of-sight velocity trend found by Müller et al. (2021) for 21 out of 28 of Cen A's satellites with measured velocities. However, the proper motion of the best-fit stream orbit in Figure 5, $(\mu_{\alpha \cos(\delta)}, \mu_{\delta}) = (0.0191, -0.0164) \text{ mas/yr},$ moves Dw3 in a direction out of Cen A's planar satellite structure (Müller et al. 2018).

^a From Hernquist (1990).

^b Relative between Cen A and Dw3.

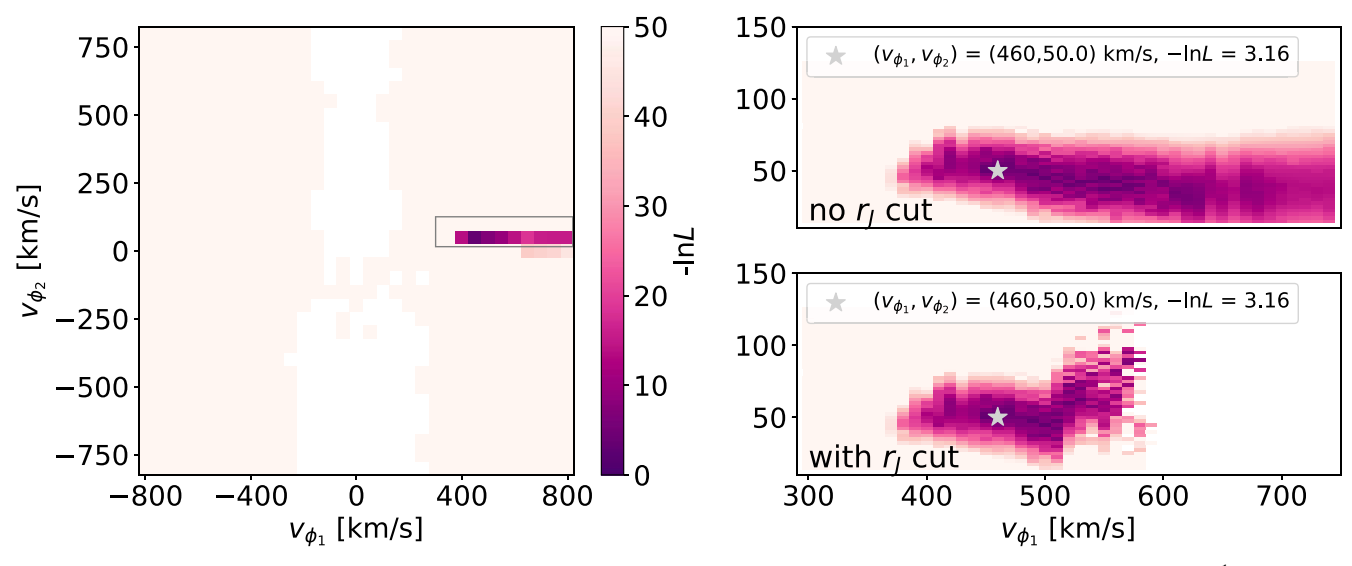


Figure 4. Summary of $-\ln \mathcal{L}$ values (Equation (2); see color bar) for model streams initiated with a fixed radial velocity of $v_{\rm rad} = -181.4~{\rm km~s}^{-1}$, but with various combinations of v_{ϕ_1} and v_{ϕ_2} . The fits of each stream to the control data are evaluated as described in Section 3.2. The blank space represents the region of the orbit parameter space, where the simulated streams were disregarded because they were shorter than the extent of the control data. Note that the maximal color bar value is $-\ln \mathcal{L} = 50$ for visualization purposes but some of the fits are extremely poor with $-\ln \mathcal{L} > 1000$. Left: A small pocket of orbits ($v_{\phi_1} \sim 300-800~{\rm km~s}^{-1}$ and $v_{\phi_2} \sim 40-100~{\rm km~s}^{-1}$) that produce good fits to the data (see gray rectangle). Upper right: Zoomed version of gray rectangle in the left panel, where we resolve the combination of v_{ϕ_1} and v_{ϕ_2} that produced good fits to the data before any Jacobi criterion is applied. Lower right: Same as above, but after the Jacobi criterion has been applied. The model stream that produced the best fit has $v_{\phi_1} = 460~{\rm km~s}^{-1}$ and $v_{\phi_2} = 50~{\rm km~s}^{-1}$ with $-\ln \mathcal{L} = 3.16$ in both cases.

 Table 4

 Summary of the Best Fit in the Fiducial Halo

Parameter	Value	Unit	
$(v_{\phi_1}, v_{\phi_2}, v_r)$	(460,50, -181.4)	[km s ⁻¹]	
$-\ln\mathcal{L}$	3.16		
Number of peri passes	2		
v _{rad} -range ^a	-116.0 - 244.5	$[\text{km s}^{-1}]$	
Distance range ^a	100.6–55.4	[kpc]	

Note.

4.2. Verifying the Best Fit with an N-body Code

We explore whether the best-fit Dw3 stream can be reproduced under more realistic stellar stripping conditions with the GCD+ (Kawata & Gibson 2003) *N*-body code (see Section 3.5 for the detailed setup of the simulation). We initialized the simulation from the end point of the 6 Gyr orbit for the best-fit model stream in the fiducial halo, where (x, y, z) = (-128.999, 170.042, -43.190) kpc and $(v_x, v_y, v_z) = (-3.378, -279.266, -158.709)$ km s⁻¹, and then we integrated Dw3 forward in the fiducial potential for 6 Gyr to its present-day position.

In Figure 6, we show the results of the comparison between the model stream from Figure 5 in Cen A galactocentric coordinates (top) and for the GCD+ (Kawata & Gibson 2003) N-body run in galactocentric coordinates (bottom) at present day. We find that the dark matter (blue particles) extends beyond the stellar component (inferno color map), as expected. The morphology of the stellar streams produced in both the Fardal et al. (2015) model stream case (top) and the N-body run (bottom) are very similar. The Dw3 position at present day is marked with a white star in the top panel, and it is visible as an overdensity of stars in the bottom panel. For this particular run, we find there to be $1.4 \times 10^7~M_\odot$ stars and $7.4 \times 10^7~M_\odot$ dark

matter remaining within 5 kpc of the Dw3 remnant in the *N*-body run at present day. This stellar mass is lower than the present-day observed mass of the remnant, but these numbers depend on the detailed setup of Dw3 and could be fine-tuned to better match to the data (see Section 3.5). While the presence of dark matter in the Dw3 remnant changes the exact escape conditions, which are also more simplistic in the model stream case (see Section 3.3), we conclude that the Fardal et al. (2015) model streams produce good approximations to the Dw3 stellar stream evolution.

4.3. Halo Mass versus Stream Morphology Degeneracy

Our goal is to test whether the Dw3 stream can provide limits on the dark matter halo mass distribution of Cen A. But before we start, it is important to understand the degeneracies that exist between dark matter halo mass and the properties of the progenitor's orbit, mass, and resulting stream morphology.

In Figure 7, we simulate a stream with an orbit similar to that of the best-fit stream in Figure 5, now in the galactic coordinate system of Cen A (see Section 3.2) in both the fiducial dark matter halo (see upper left panel), as well as in an NFW dark matter halo with a fourth of the mass, but for a fixed scale radius. In the case of Dw3 in Cen A's halo, we know the projected distance between Cen A and the dwarf. We have therefore initiated the two streams with the same physical separation from Cen A's center. The difference between the high-mass (left) and low-mass (right) progenitor orbits, is that the right stream, evolved in the lower-mass halo, has a velocity scaled down by a factor of two compared to the left. The enclosed mass difference at pericenter for the left and right scenarios is a factor of four smaller for the low-mass halo (right). In this example, we therefore scaled down the Dw3 progenitor mass by a factor of four in the low-mass halo (right) and integrated for twice as long (see Johnston et al. 2001, for an analytic expression of these scalings in a logarithmic potential).

^a Listed with respect to Cen A's rest frame from the most northern control data point to the most southern control data point.

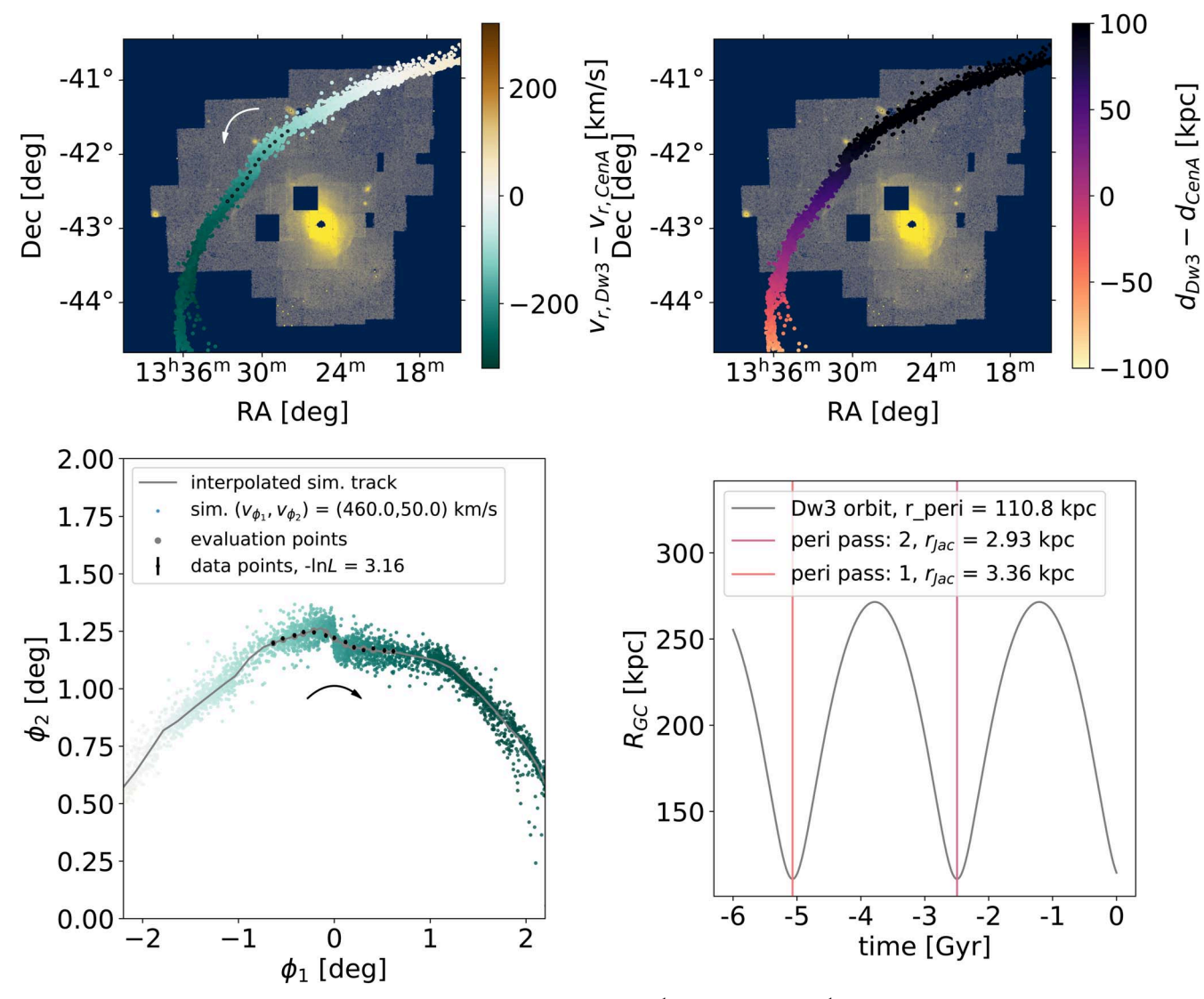


Figure 5. Visualization of the best-fit model stream from Figure 4 with $v_{\phi_1} = 460 \text{ km s}^{-1}$ and $v_{\phi_2} = 50 \text{ km s}^{-1}$ and $-\ln \mathcal{L} = 3.16$. Upper panels: The model stream transformed to ICRS coordinates, colored by radial velocity in Cen A's rest frame (left) and distance along the stream with respect to Cen A (right), overplotted on the Cen A image data. The white arrow indicates the direction of motion of Dw3, and the black points are the 13 control data points, x_n (see also orange points in Figure 1). Lower left: The best-fit model stream shown in (ϕ_1, ϕ_2) space in degrees (see Section 3.2). The orange points are the 13 control data points, x_n , the green points (colored by radial velocity) are the simulated model stream, the gray line is the center point of the simulated model stream, and the gray dots are the 13 simulated stream center points, y_n , at the ϕ_1 location of the control data. The black arrow indicates the direction of motion of Dw3. Lower right: The evolution of the 3D position in kpc of the progenitor with respect to Cen A's center as a function of time (black line, t = 0 at present day). The vertical lines mark the pericenter passages of the progenitor.

We find that the morphologies of the two streams are identical in the high-mass versus the low-mass case in Figure 7 (except for scatter induced by the stream-modeling technique). The apocenter and pericenter distance with respect to Cen A's center (lower panels) and the tidal radius at present day are also identical (in this toy example, we do not assume any mass loss of the progenitor). However, the radial velocities of the two streams are very different (see color bar). While the stream evolved in the fiducial halo (left) has a radial velocity of -181.4 km s^{-1} , Dw3, evolved in the lower-mass halo, needs to have lower radial velocity by a factor of two $(-90.7 \text{ km s}^{-1})$ in order to reproduce the same morphology. Thus, knowing just the one radial velocity of Dw3 helps break the halo mass versus stream morphology degeneracy. Note also how the radial velocities along the streams are very different in the two scenarios.

4.4. Varying the Halo Mass

To test the constraining power of the Dw3 stream on Cen A's halo mass, we explore whether the Dw3 stream can be reproduced in the 10 different potentials shown in Figure 2 (see also Table 2). We test if there is a lower limit on the halo mass in which the stream morphology cannot be reproduced, given the observational constraint of the radial velocity of Dw3 ($v_{\rm rad} = -181.4~{\rm km~s^{-1}}$; Dumont et al. 2022). As we do not expect the nature of the orbital solution to change due to a change in halo mass (see Figure 7), we use the same velocity resolution in v_{ϕ_1} , v_{ϕ_2} (i.e., stepping 10 km s⁻¹ in v_{ϕ_1} and 2.5 km s⁻¹ in v_{ϕ_2}) as presented in Figure 4, but spanning a larger range in velocities in order to capture the differences in each halo. For each velocity combination, we generate a stream and record the $-{\rm ln}\,\mathcal{L}$ value, but now in 10 different halos. In this section, we present $-{\rm ln}\,\mathcal{L}$ values and model streams only after we apply the

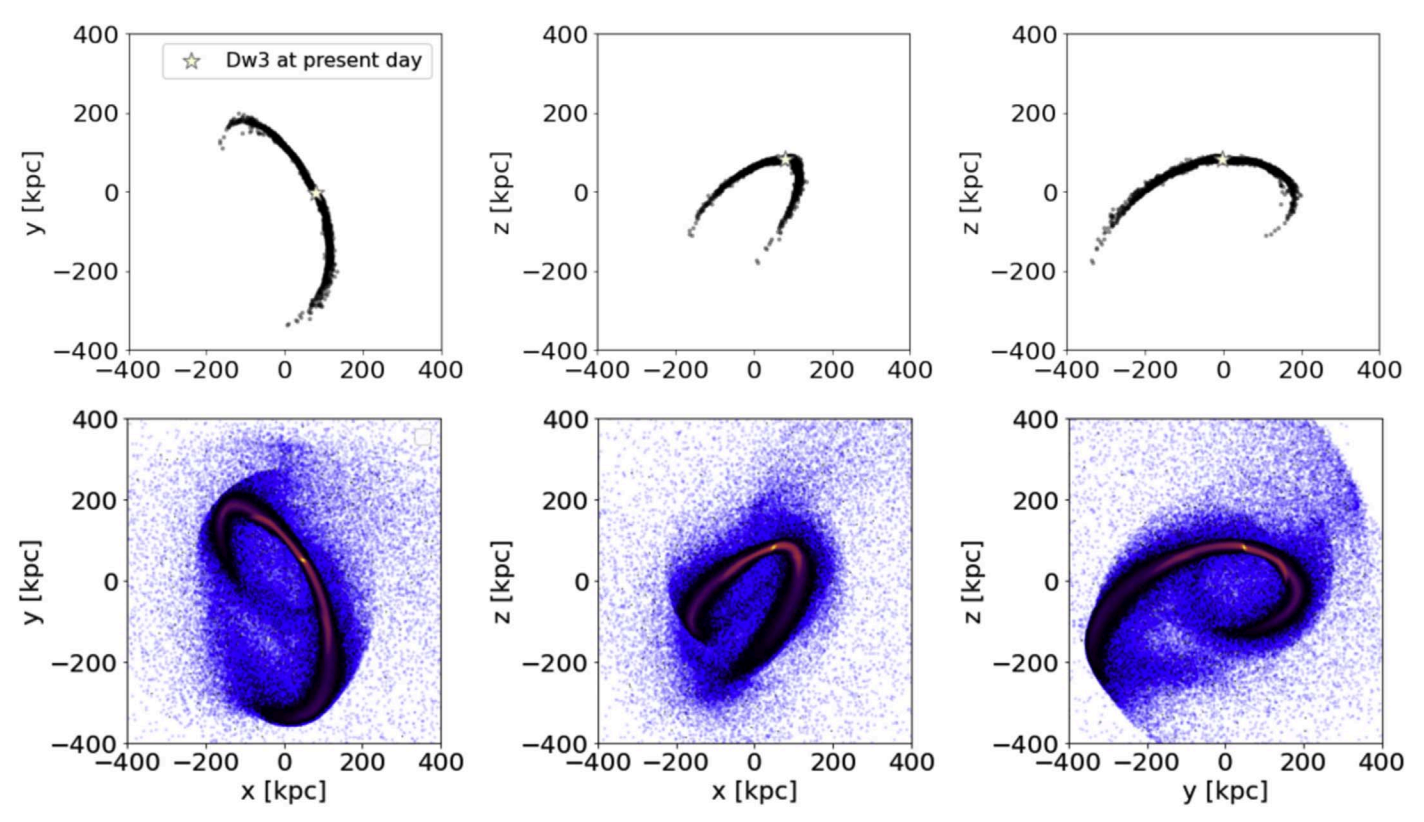


Figure 6. Comparison between the best-fit model stream evolved with the Fardal et al. (2015) mock stream generator (top) and the GCD+ (Kawata & Gibson 2003) N-body follow-up (bottom). Both runs are shown in galactocentric coordinates centered on Cen A at (x, y, z) = (0,0,0), and Dw3 was evolved for 6 Gyr in the fiducial potential in both cases. Top panels: Black particles show the stars in the model stream, and the white star marks the progenitor position at present day. Bottom panels: Blue particles show the extended dark matter, and the inferno color map shows the stars. The Dw3 remnant is visible as an overdensity of stars. The stellar component of both the model stream (top) and the N-body stream (bottom) look very similar.

Jacobi cut (see Section 3.3), to ensure physical tidal stripping conditions. We again fix the distances to Cen A, the distance to Dw3, and the radial velocity and mass profile of Dw3.

In Figure 8 (left), we show the values of $-\ln \mathcal{L}$, where dark colors indicate better fits to the control data for each velocity combination of the model streams in five of the ten different halos after the Jacobi radius cut (we skip every other halo in between, for visualization purposes). We find that the Dw3 stream cannot be reproduced in the lowest-mass halo (Halo 1: $M_{200} = 0.94 \times 10^{12} \ M_{\odot}$) because no model stream covers the extent of the data after the Jacobi cut (see top row). Similarly, in Halo 2 ($M_{200} = 2.82 \times 10^{12} \ M_{\odot}$), most of the stars are removed from the model streams after the Jacobi cut, and only very poor fits to the data exist ($-\ln \mathcal{L} > 20$). Thus, the Dw3 stream cannot be reproduced in the two lowest-mass halos.

For the rest of the halos shown in Figure 8 (left), the gray stars mark the combination of v_{ϕ_1} , v_{ϕ_2} that produced the best-fit model stream in each halo. We summarize the values of $-\ln\mathcal{L}$ in each halo in Table 2. The pockets of orbital solutions that produce good fits to the data in the different halos move to higher values of (v_{ϕ_1}, v_{ϕ_2}) for more massive halos, as expected from Figure 7, because the progenitors must move faster to produce such a straight stream in a more massive potential. The exact combination of v_{ϕ_1} , v_{ϕ_2} does not scale directly with halo mass (as in Figure 7), because the radial velocity of Dw3, the Dw3 mass, and the integration time are fixed in this experiment. Instead, the pockets of solutions shift to best reproduce the shape of the control data with a combination of v_{ϕ_1} , v_{ϕ_2} .

In the second panel of Figure 8, we show the model streams in (ϕ_1, ϕ_2) space generated with the velocity combination that produced the best fit in the left panel. Because no model stream covered the extent of the data in Halo 1 after the Jacobi cut, we show an example of an orbit with $(v_{\phi_1}, v_{\phi_2}) = (150,20) \text{ km s}^{-1}$. The control data, x_n , are shown in black, while the simulated stream center points, y_n , are shown in gray. Note that the gray center points for the simulated streams are difficult to see when they overlap well with the control data points in black.

In the third panel, we show the 3D physical separation between Dw3 and Cen A's center as a function of time. Note that the model stream for Halo 1 (top) is on the first infall. The best-fit stream in Halo 3 has only had one pericenter pass. In all other halos, Dw3 has completed two or more pericenter passes by the present day. In the right panels of Figure 8, we show the best-fit streams, but in ICRS coordinates projected onto the image data of Cen A and colored by the radial velocity in Cen A's rest frame (see color bar in Figure 5).

The lowest halo mass of Cen A in which we can fit the stream of Dw3 is Halo 3 (second row in Figure 8), which has $M_{200} = 4.70 \times 10^{12} M_{\odot}$ (see also Table 2). However, the fit in this halo is poor $(-\ln \mathcal{L} = 7.83)$ compared to those of the higher-mass halos $(-\ln \mathcal{L} < 4)$.

To check if the poorer fit in Halo 3 is due to a resolution issue, we rerun a grid of orbits for Halo 3, stepping in increments of 2.5 km s⁻¹ in v_{ϕ_1} and 1 km s⁻¹ in v_{ϕ_2} instead. With the finer velocity resolution, we found a fit in Halo 3 that had $-\ln \mathcal{L} = 7.35$, where $(v_{\phi_1}, v_{\phi_2}) = (345, 47)$ km s⁻¹. While this fit is worse than the fits for Halo 4 through 10 (see

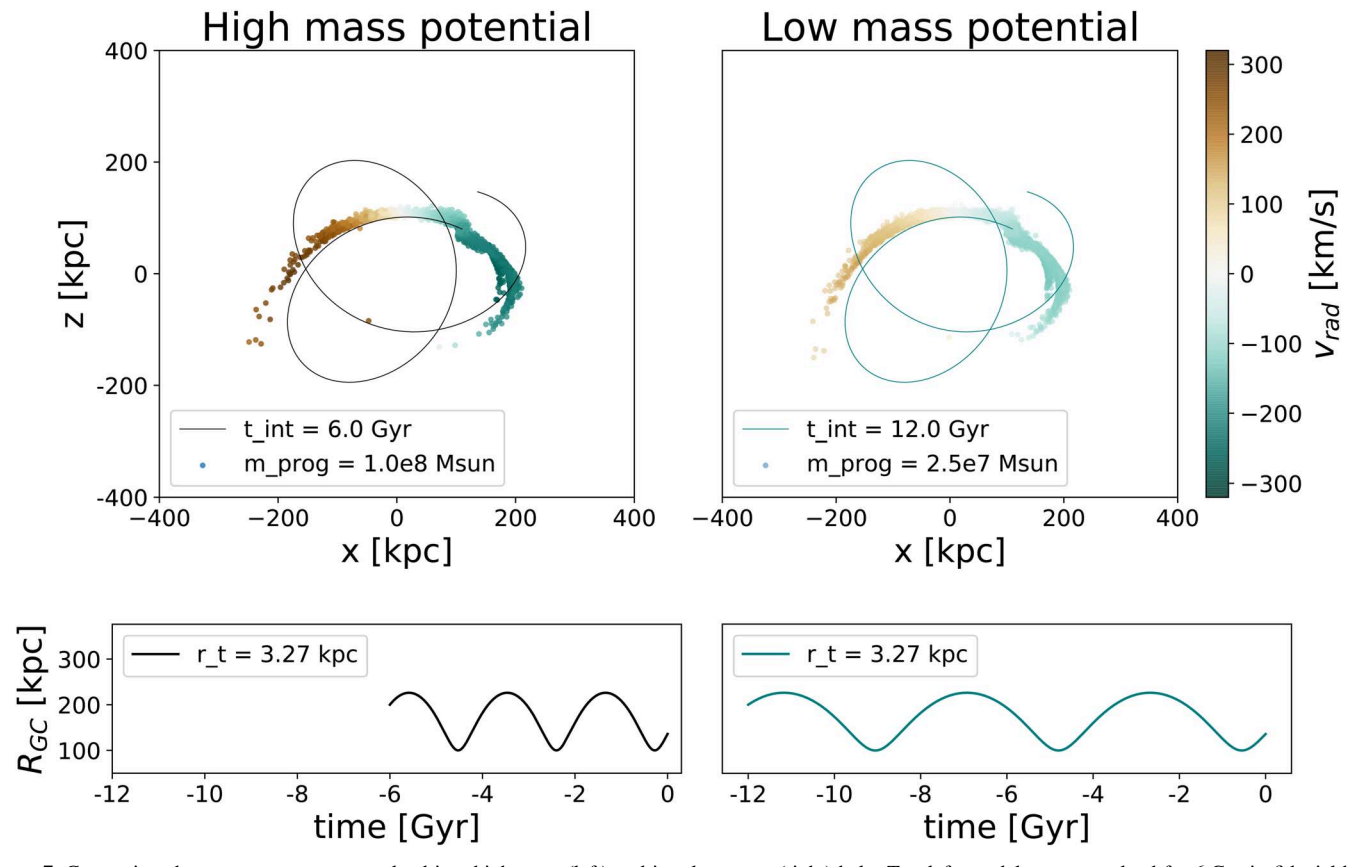


Figure 7. Comparison between two streams evolved in a high-mass (left) and in a low-mass (right) halo. Top left: model stream evolved for 6 Gyr in fiducial halo (colored by radial velocity in Cen A's rest frame) and progenitor orbit (black line) projected in x and z galactic coordinates in kpc, where Cen A is located at (x, z) = (0,0). The progenitor has an initial mass of $10^8 \, M_\odot$. Top right: Model stream evolved for 12 Gyr in a halo mass scaled down by a factor of four as compared to the fiducial halo. The teal line shows the orbit of the progenitor. The progenitor mass in the right panel is also scaled down by a factor of four, and its orbital velocity is scaled down by a factor of two. The two streams have identical morphologies but very different radial velocities. Bottom left: The model stream's 3D galactocentric distance with respect to Cen A's center as a function of time. Bottom right: Same as bottom left, but now for the progenitor with a fourth of the mass and half of the orbital velocity. Note how the tidal radius, pericenter, and apocenter distances are identical in the two cases.

Table 2), we do not disregard this halo as a viable dark matter potential for Cen A.

The lower limit of $M_{200} > 4.70 \times 10^{12} M_{\odot}$ (Halo 3) was constrained by only the one radial velocity measurement of Dw3 from Dumont et al. (2022). We notice, however, that the velocity gradient for a fixed distance from Dw3 also varies along the stream for the best fits (see colors in panels 2 and 4 of Figure 8).

To explore this further, in Figure 9 we show the velocity gradients (left) and distance gradients (right) of each of the best-fit simulated streams in the halos for which we could find a decent match to the control data (Halo 3 through Halo 10). In particular, we have evaluated the radial velocity and line-of-sight distance of the model stream simulations at the ϕ_1 location of the 13 control points in the simulations and plotted a line through each point for each best-fit model stream.

The radial velocity gradients (left) all cross at $v_{\rm rad} = -181.4$ km s⁻¹, because this velocity of Dw3 was fixed for all model stream simulations. Note how the radial velocity gradient along the stream gets steeper with higher halo masses (see blue line), as the stream needs to move faster to be on the same type of orbit. The radial velocity contrasts are larger at the edge of each stream, where the difference between Halo 3 (red; least massive) and Halo 10 (blue; most massive) is ~10 km s⁻¹. If we could measure radial velocities along the stream (see, e.g.,

Toloba et al. 2016a), in particular at the end points of the streams, we could further constrain the dark matter halo mass.

The distance to Dw3 has been fixed to 3.88 Mpc, and Cen A's distance has been fixed to 3.8 Mpc. Thus, all line-of-sight distances (Figure 9, right) cross at a relative distance of 80 kpc. We find that the distance gradient is shallower in the highest-mass halo (blue line) and that observations of distances at the end points of the streams could further constrain the dark matter halo mass. Both the radial velocity gradients and line-of-sight distance gradients are technically observable (see Section 5.1 for a discussion of the feasibility of such measurements and their observational errors).

5. Discussion

We have shown that, with just one radial velocity measurement of a stream progenitor combined with the sky track of an extragalactic stream, we can constrain properties of the dark matter halo of Cen A. In this section, we discuss progenitor distance degeneracies (Section 5.1) as well as other degeneracies (Section 5.2), we compare our new Cen A halo constraints to other existing limits (Section 5.3), we discuss the effect of including multiple Cen A streams in Section 5.4, and we discuss the future of external galaxy stream science as well as how to maximize the dark matter science output of these structures in Section 5.5.

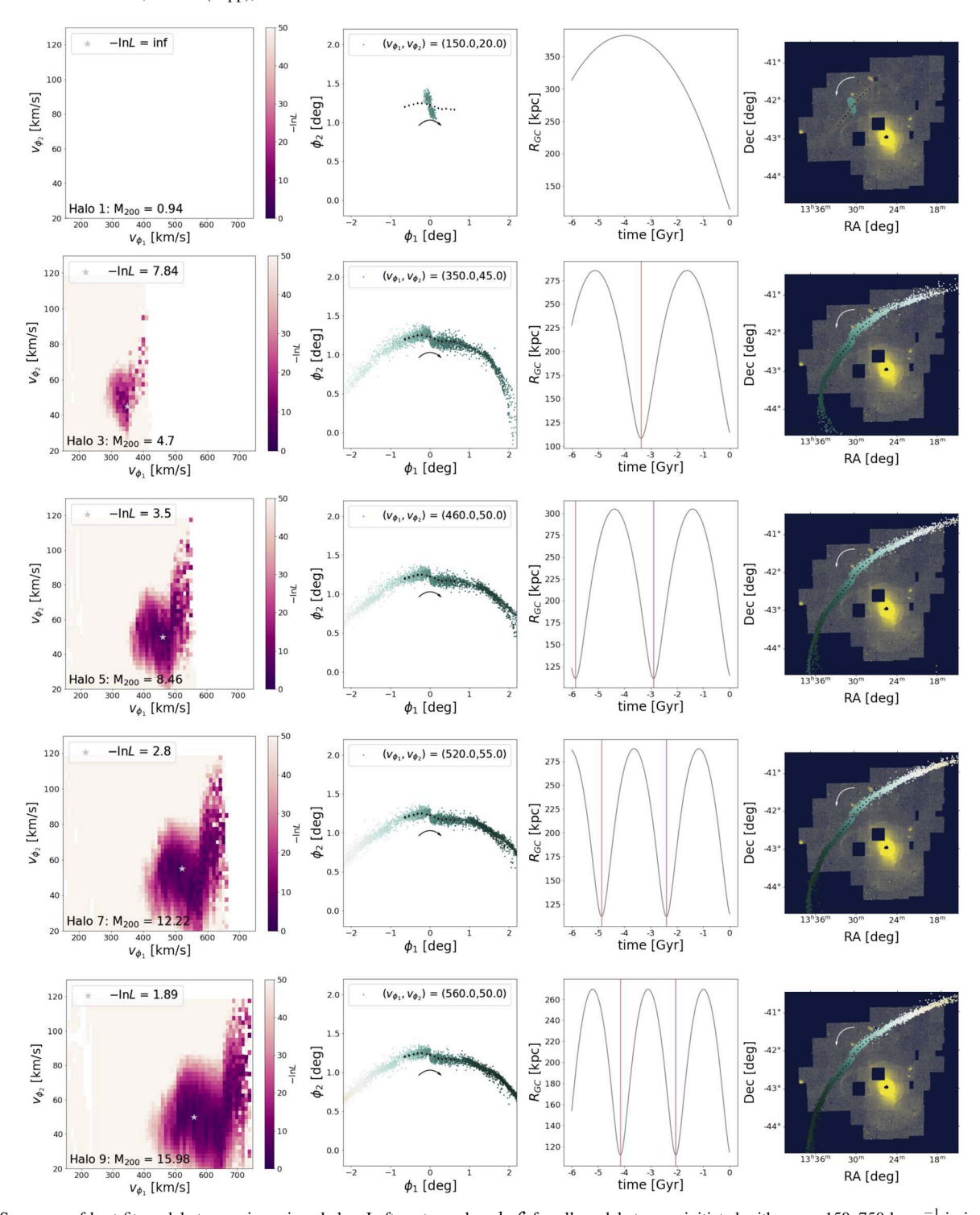


Figure 8. Summary of best-fit model streams in various halos. Leftmost panels: $-\ln \mathcal{L}$ for all model streams initiated with $v_{\phi_1} = 150-750 \text{ km s}^{-1}$ in increments of 10 km s^{-1} and $v_{\phi_2} = 20-120 \text{ km s}^{-1}$ in increments of 2.5 km s^{-1} evolved for 6 Gyr in five different dark matter halos. The Jacobi radius cut has been applied in all panels (see Section 3.3). All M_{200} values are listed in units of $10^{12} M_{\odot}$. The gray stars mark the combination of orbital parameters (v_{ϕ_1}, v_{ϕ_2}) that produced the best-fit model stream in each halo. Dark colors indicate pockets of best-fit solutions (see color bar in Figure 4). Blank spaces in the left parts of the panels indicate orbits for which the model stream did not cover the extent of the data after the Jacobi cut. Middle left panels: Visualization of the best-fit model stream in (ϕ_1, ϕ_2) space in each halo after the Jacobi radius cut, colored by the radial velocity along the stream in Cen A's rest frame (see colorbar in Figure 5). For Halo 1 (top), the model stream does not cover the extent of the data for any orbit after the Jacobi cut, so we show an example of an orbit with $(v_{\phi_1}, v_{\phi_2}) = (150,20) \text{ km s}^{-1}$. The black points show the 13 control data points (x_n) , and the gray points, (y_n) , show the model stream center points at the ϕ_1 location of the control data (note that these are hard to see when the control data points overlap well with the center points of the simulated stream). The black arrows indicate the direction of motion of each model stream. Middle right panels: The 3D position of Dw3 with respect to Cen A's center as a function of time. Rightmost panels: The best-fit model streams colored by radial velocity in Cen A's rest frame and presented in ICRS coordinates, overplotted on the Cen A image data. The white arrows indicate the direction of motion for each model stream.

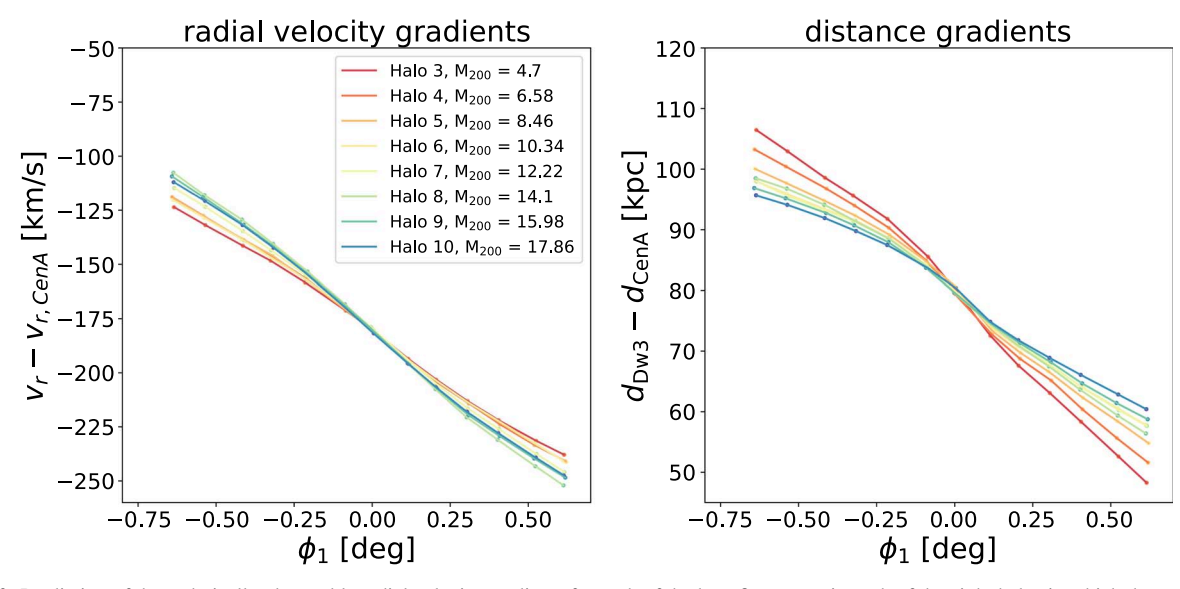


Figure 9. Left: Prediction of the technically observable radial velocity gradients for each of the best-fit streams in each of the eight halos in which the stream could be well-fit after applying the Jacobi criterion. All M_{200} values are listed in units of $10^{12} M_{\odot}$. The radial velocities are evaluated at the ϕ_1 locations of the 13 control data points, x_n (see dots), for each best-fit model stream. The best-fit model streams in the more massive halos have steeper velocity gradients. Right: Same as the left panel, but now for the line-of-sight distance gradient with respect to Cen A along each best-fit stream in each of the eight halos. The best-fit model streams in the more massive halos have shallower distance gradients along the streams.

5.1. Distance versus Radial Velocity Degeneracy

If we did not know the distance to Dw3, we could produce a similar fit to the stream in the fiducial halo if we placed the dwarf in front of Cen A. To demonstrate this, we first use the orbital solution of the best fit from Figure 5 in the fiducial halo (see Table 4) and then create an array of distances to Dw3 from -400 to 400 kpc in increments of 15 kpc with respect to Cen A located at 3.8 Mpc. We generate model streams where we place Dw3 at each of these distances, and we record the value of $-\ln \mathcal{L}$ for each model stream compared to the data.

In the top panel of Figure 10, we plot the $-\ln \mathcal{L}$ value as a function of Dw3 distance for each model stream. There are two clear minima (see labels A and B), which correspond to the two best fits to the control data points. The first minimum (A) is when Dw3 is closer to us than CenA, at $d=-76\,\mathrm{kpc}$ (see gray dashed line), and the second minimum (B) is when Dw3 is farther from Cen A, at $d=76\,\mathrm{kpc}$. In the two lower left panels, we visualize the best-fit model stream in front of Cen A in ICRS coordinates overplotted on the image data of Cen A, where the stream is colored by the radial velocity along the stream in Cen A's rest frame (top) and colored by the distance gradient along the stream (bottom). In the lower right panels, we show the same plots, but for the Dw3 solution at a distance further away than Cen A.

While the signs of the distance gradients are the same for the two fits (the southern parts of the stream are in the foreground of Dw3 in both cases), the signs of the radial velocities flip in the two cases. For case A, where Dw3 is closer to us than Cen A, the stream is moving toward us with respect to Cen A in the southern parts. For case B, where Dw3 is farther from us than Cen A, the stream is receding from us with respect to Cen A in the southern parts. Thus, if we can observe just the sign of the velocity gradient along the stream, this is a strong indicator of whether Dw3 resides behind versus in front of Cen A.

The model streams clearly predict that the northern part of the stream should be farther than Dw3 in both cases, and that the radial velocity gradient should be decreasing from north to south if Dw3 resides "behind" Cen A. Using the tip of the redgiant branch method, Crnojević et al. (2019) present distances along Dw3's stream from HST data (see their Table 5). For three pointings, one placed on Dw3 and two placed in the northern and southern parts of the stream, respectively (see pointings in their Figure 13), the data from the ACS fields show that the southern part is closer to us than Dw3 and that the progenitor distance and the northern stream distance are very similar (which resembles both of our cases in Figure 10). However, within the errors of their measurements, the three pointings are all consistent with being at the same distance. With larger field of views (e.g., with the Roman space telescope), however, a large fraction of the stream can be covered in one field, which might help determine continuous changes in distance along the stream and whether the northern part is in fact farther from us than Dw3.

While it is encouraging that the best-fit distance behind Cen A, d = 76 kpc, is close to the actual observed relative distance between Cen A and Dw3 of 80 kpc, recall that in the test in Figure 10, we have used the best-fit orbit (see Table 4) for that specific $d_{\mathrm{Dw3}} = 3.88\,\mathrm{Mpc}$ distance. Thus, the fact that we obtain a similar distance is not surprising. Similarly, it is not surprising that Case B produces a better fit $(-\ln \mathcal{L}_B = 3.52)$ than Case A ($-\ln \mathcal{L}_A = 9.33$) for that same best-fit orbit. When we run a grid of orbits for model streams where Dw3 is placed in front of Cen A (at d = -76 kpc with respect to Cen A), we find equally good fits to the data as in Case B. The radial velocity gradients in the fits where Dw3 is behind versus in front of Cen A have the opposite sign, while the distance gradients have the same sign (as expected from Figure 10). We emphasize again how an observation of just the sign of the velocity gradient is very informative.

5.2. Other Degeneracies and Limitations of Our Method

Throughout this work, we have fixed certain parameters. Here, we discuss how these decisions affect our results.

1. Integration time: When we evaluate the fits to the data, we have discarded model streams that do not cover the extent of the 13 control points after 6 Gyr of evolution.

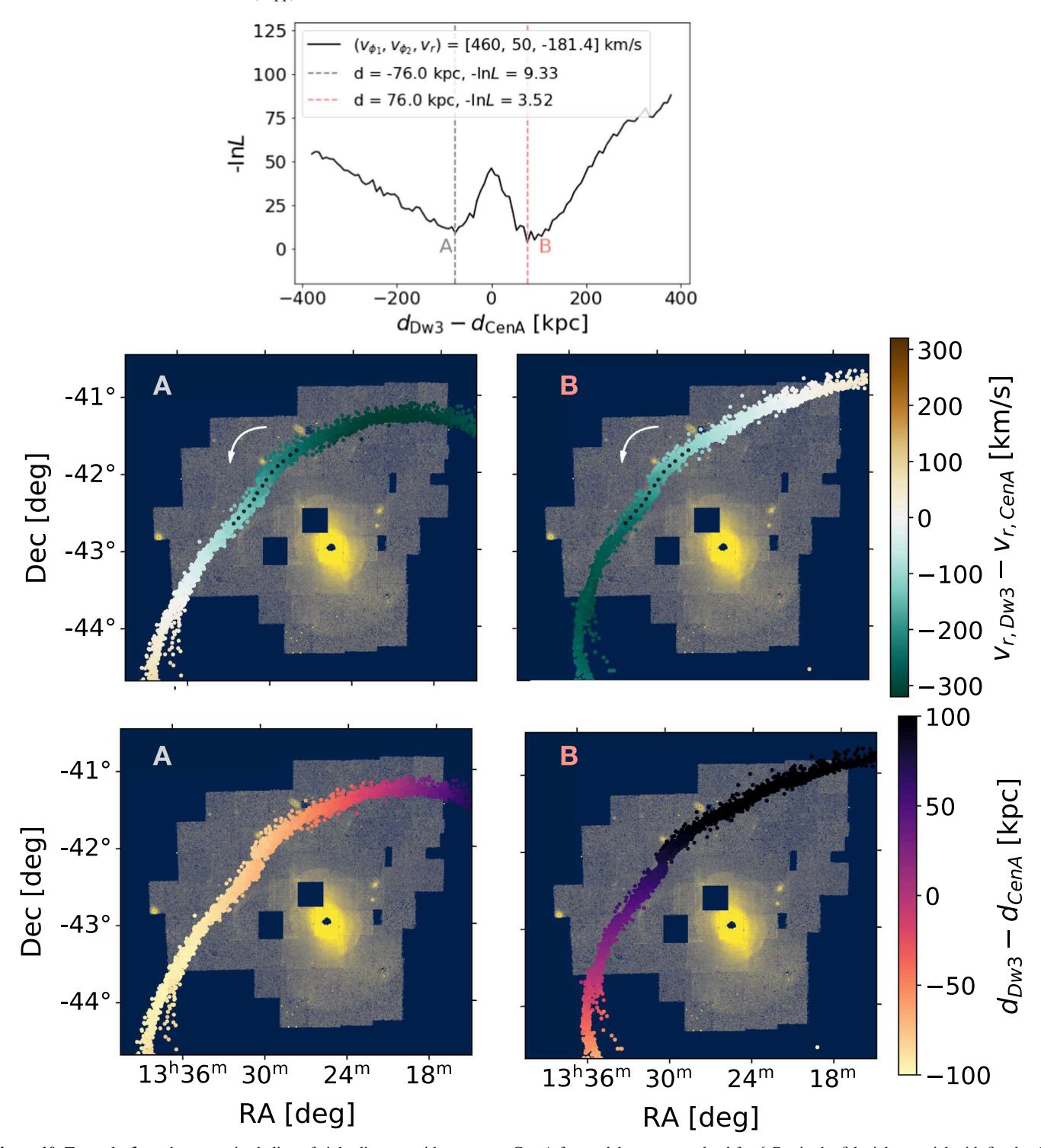


Figure 10. Top: $-\ln \mathcal{L}$ vs. the progenitor's line-of-sight distance with respect to Cen A for model streams evolved for 6 Gyr in the fiducial potential with fixed radial velocity, progenitor mass, and fixed $(v_{\phi_1}, v_{\phi_2}, v_r) = (460, 50, -181.4)$ km s⁻¹ from the best-fit model stream presented in Figure 5. There are two clear minima (best fits), located in front of (A: d=-76.0 kpc) and behind (B: d=76.0 kpc) Cen A (which is at 3.8 Mpc). Middle: Visualization of the model streams in ICRS coordinates from the best fit in front of (A: left) and behind (B: right) Cen A overplotted on the Cen A image data and colored by the radial velocity in Cen A's rest frame. Note how the radial velocities flip direction in the two cases. Bottom: same two model streams, but now colored by distance along the stream with respect to Cen A. The distance gradients in the southern part of the model streams are closer to us than the northern part in both cases.

However, if we integrate some of those disregarded streams for a longer period, it is possible that they could cover the extent of the data. ¹⁰ To check how different

integration times affect our results, we rerun the grid of $(\nu_{\phi_1},\nu_{\phi_2})$ velocities in Figure 4, but integrate the model stream orbits and release stream stars for 4 Gyr and 8 Gyr instead of 6 Gyr. We find that some of the regions with high $-\ln\mathcal{L}$ values (see color bar in Figure 4) move toward lower values (better fits) for the 8 Gyr integration

 $[\]overline{^{10}}$ Note that some model streams point in the radial direction and that a longer integration time would not help in these cases.

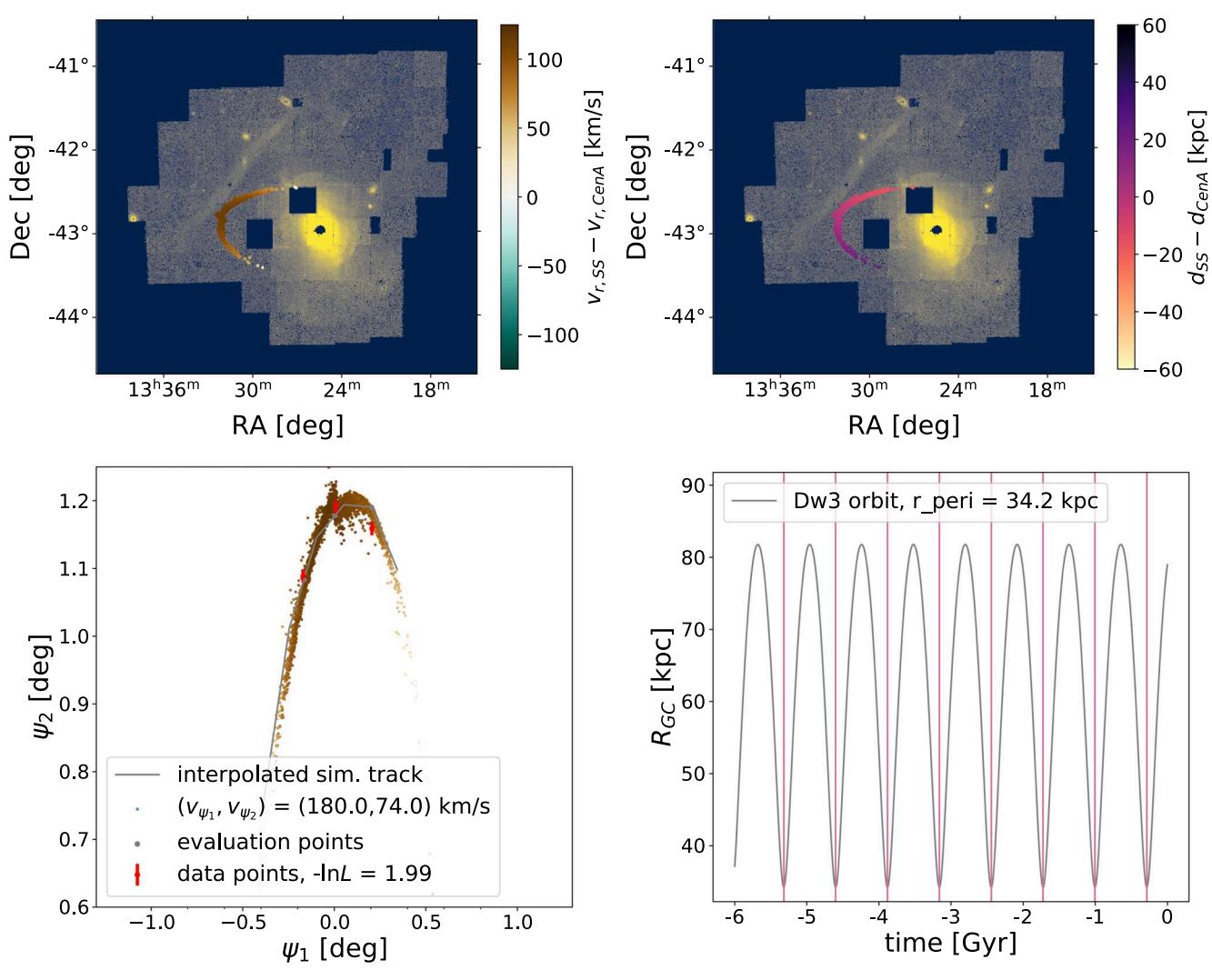


Figure 11. The best fit to the three control data points of the "second stream" (SS) in Cen A's halo evolved in the fiducial potential integrated for 6 Gyr. We fix the radial velocity to 110 km s⁻¹ with respect to Cen A's rest frame and find that $(v_{\psi_1}, v_{\psi_2}) = (180,74)$ km s⁻¹ minimizes $-\ln \mathcal{L}$ to be 1.99. Upper panels: ICRS projection of the best-fit simulated stream overplotted on the Cen A image data colored by the radial velocity in Cen A's rest frame (left) and the distance along the stream with respect to Cen A's distance (right). Bottom left: the best-fit stream visualized in (ψ_1, ψ_2) space. The red points are the three control data points. The gray points are the center points of the simulated stream evaluated at the ψ_1 position of the control data points. Bottom right: galactocentric 3D position of the simulated progenitor as a function of time.

time, and some of the regions with low $-\ln \mathcal{L}$ values (see color bar in Figure 4) move toward higher values (worse fits) for the 4 Gyr integration time. However, this does not change our main best-fit orbital solution. A more important factor than the integration time is the fraction of the orbital time during which the progenitor can actually tidally strip stars (see Equation (1)).

- 2. Progenitor mass: In Figure 7, we showed that, if we simulated Dw3 in a lower-mass halo but integrated its orbit for longer with a lower progenitor mass and orbital velocity, we could reproduce the same morphology of the stream as in a more massive halo. Thus, if we lower the mass of the progenitor and lower the orbital velocity but prolong the integration time, we could potentially produce solutions similar to our best fit. However, because we have a radial velocity measurement of Dw3, we cannot arbitrarily scale down the orbital velocity. A good constraint on the progenitor mass does help break degeneracies on integration time, and it also affects the Jacobi radius in a specific halo (see
- Equation (1)). If the progenitor had a higher initial mass, some of which can be in the form of dark matter (see Section 4.2), it would be harder to strip stars from the dwarf. A more massive Dw3 would need to be evolved in an even higher Cen A halo mass to have its stars stripped. Thus, the lower limit presented in this work would only become even more constraining in that case. A higher progenitor mass would also affect the width of the stream, which has been left as a free parameter in this work.
- 3. Cen A distance: Throughout this work, we have fixed the distance to Cen A to 3.8 Mpc, which sets the physical scale of our coordinate system. If Cen A instead were closer to us, this would lead to a smaller physical projected separation between Dw3 and Cen A (instead of 79 kpc). If we use the same best-fit velocity as in Figure 5, Dw3 would complete more orbits and reach a smaller pericenter, and therefore the tidal radius would also be smaller. This would, in turn, change our limits on the minimum halo mass. However, the error on the distance estimate for Cen A for Harris et al. (2010) is

- $d = 3.8 \pm 0.1$ Mpc, so this is a minimal effect, although we might have larger distance uncertainties for smaller dwarf galaxies or more distant, less studied galaxies in future analyses.
- 4. NFW potentials: We primarily use the fiducial potential (see Section 3.1) motivated by enclosed mass estimates from GCs, and we also explore a range of 10 potentials with $[0.1-1.9] \times M_{200,\mathrm{fiducial}}$. In this work, the lower limit on the dark matter halo mass for Cen A is determined from the minimum halo mass of those 10 potentials in which the straight Dw3 stream's control data could be reproduced. However, an exploration of the lower limit through a finer range of NFW potentials could yield a better lower limit. Given the limitations listed above, we do not explore more potentials in this work.
- 5. Time dependence: We have assumed that the potential of Cen A is static. From recent work on stellar streams in the Milky Way (e.g., Shipp et al. 2021; Dillamore et al. 2022; Lilleengen et al. 2022), we know that both thin GC streams and dwarf galaxy streams are sensitive to perturbations from accreted dwarf galaxies (see also the LMC's effect on the Milky Way's dark matter halo in Garavito-Camargo et al. 2019). Nibauer et al. (2022) argue that not all streams are sensitive to such perturbations (depending on the streams' orbits with respect to the infalling satellite's orbit) and that some streams can still provide powerful constraints on dark matter halo parameters despite their time dependence. It is unclear how much the assumption that Dw3 evolves in a static potential for 6 Gyr used in this work affects our results.

5.3. Comparison to Other Dark Matter Halo Mass Limits

After exploring a range of NFW potentials to represent Cen A's dark matter halo, we found that the straight stream from Dw3 can be reproduced in a potential with an NFW profile with $M_{200}>4.70\times10^{12}~M_{\odot}$. Using 3D distances, line-of-sight velocities, and a Bayesian model to study the kinematics of the satellite systems of Cen A, Müller et al. (2022) derive $M_{200}=5.3\pm3.5\times10^{12}~M_{\odot}$, similar to our limit within the errors.

Peng et al. (2004) reported Cen A's enclosed mass at 40 kpc ($\sim 36'$), using 215 GCs to be $M(R < 40 \, \mathrm{kpc}) = 7.5 \times 10^{11} \, M_{\odot}$ (see Woodley et al. 2007, for this corrected mass). For comparison, Woodley et al. (2010) set a limit on the enclosed mass of $M(R < 40 \, \mathrm{kpc}) = 9.7 \pm 3.3 \times 10^{11} \, M_{\odot}$, using 429 GCs in Cen A. In this work, the potential with the minimal halo mass (Halo 3) that could reproduce the straight stream from Dw3 has $M(R < 40 \, \mathrm{kpc}) = 7.21 \times 10^{11} \, M_{\odot}$ (see Table 2). Overall, the lower limit on the dark matter halo mass provided in this paper is in agreement with previous studies.

5.4. What about Cen A's Other Substructure?

In addition to the stream emerging from Cen A, there are several shell features and a prominent "second stream" (see Figure 1) present in the data. Wang et al. (2020) showed that a single major merger event 2 Gyr ago with a mass ratio of up to 1.5 can account for much of the shell structure in the halo, and in some cases can produce features mimicking the Dw3 stream and the "second stream." In this section, we investigate the "second stream" as an individual stream originating from a dwarf galaxy progenitor. Crnojević et al. (2016) find that the

second stream is at the same distance as Cen A. For the remainder of this section, we place both Cen A and the second stream progenitor at 3.8 Mpc. There is no public radial velocity estimate, but Hughes et al. (2022) find a GC at the center of the stream with $v_{\rm rad} = 651 \pm 13$ km s⁻¹, i.e., redshifted by 110 km s⁻¹ with respect to Cen A.

It is not surprising that we can easily find an orbit that reproduces the morphology of the second stream in the Cen A fiducial halo (black line in Figure 2). To search for the best fit, we first place three control data points along the stream. We assume that the progenitor is at the center of the stream and place two other control points in the leading and trailing arms to evaluate how well the model streams fit the data (see white points in Figure 1). Note that it is unclear which arm is trailing and which is leading. We fix the radial velocity to $v_{\rm rad}$ = 110 km s⁻¹ in Cen A's rest frame. We again define a new coordinate system here (ψ_1 and ψ_2 , in degrees). We first shift the coordinate system such that Cen A is at $(\psi_1, \psi_2) = (0, 0)^{\circ}$, and then we rotate the coordinate system by 82°, such that the progenitor is located at $\psi_1 = 0$, directly above Cen A. We again use the Astropy coordinate transformation machinery (Astropy Collaboration et al. 2013, 2018) to transform the ICRS coordinates (see Table 1) of the second stream to kpc for stream modeling.

We fix the distance to the progenitor (see Table 1) and explore a grid of velocities in the v_{ψ_1} and v_{ψ_2} direction of the second stream. We first integrate the progenitor orbit for 6 Gyr for each orbit combination on a velocity grid ranging from -300 to 300 km s⁻¹ in steps of 25 km s⁻¹ in both v_{ψ_1} and v_{ψ_2} . There is a pocket of solutions that have the stream moving with either both positive or both negative v_{ψ_1} and v_{ψ_2} combinations. To resolve the best fit, we run a zoomed-in version of the peak near $v_{\psi_1} = 150$ –250 km s⁻¹ in steps of 10 km s⁻¹ and $v_{\psi_2} = 40$ –100 km s⁻¹ in steps of 2 km s⁻¹. Note that no stars are removed with the Jacobi cut for these orbits in this fiducial potential.

The best fit is for $(v_{\psi_1}, v_{\psi_2}) = (180, 74) \text{ km s}^{-1}$, where $-\ln \mathcal{L} = 1.99$, which we present in Figure 11. Note that there was a very similar fit where the stream moved in the negative (v_{ψ_1}, v_{ψ_2}) direction. In the top panels, we show the stream projected in ICRS coordinates overplotted on the Cen A image data colored by the second stream's simulated radial velocity gradient in Cen A's rest frame (left) and distance gradient with respect to Cen A (right). Our best-fit model stream shows a very flat velocity gradient, where the ends of the stream are slightly less redshifted with respect to Cen A. We plot the model stream in the $\psi_1, \ \psi_2$ space (lower left), as well as the evolution of the 3D position of the progenitor with respect to the center of Cen A (lower right). The progenitor is close to apocenter today. We find a very similar best fit in the minimum halo mass that could reproduce the Dw3 stream (Halo 3: $M_{200} = 4.7 \times 10^{12} M_{\odot}$): $(v_{\psi_1}, v_{\psi_2}) = (150, 64) \text{ km s}^{-1}$, with $-\ln \mathcal{L} = 2$, as well as in the lowest-mass halo (Halo 1: $M_{200} = 9.4 \times 10^{11} M_{\odot}$): $(v_{\psi_1}, v_{\psi_2}) =$ $(90, 44) \text{ km s}^{-1}, \text{ with } -\ln \mathcal{L} = 2.32.$

Bonaca & Hogg (2018) found that multiple streams in one halo have greater constraining power on dark matter halos. We plan to extend the method of Bonaca & Hogg (2018) to external galaxies and explore the information content of multiple extragalactic streams observed in projection. We leave any further exploration, in particular of the second stream and the Dw3 stream's combined constraining power on the Cen A halo concentration and shape, for future work.

5.5. The Future of Extragalactic Streams for Dark Matter Science

Extragalactic stellar streams offer one of the few methods for measuring the dark matter halos in individual galaxies. Observing radial velocities of low surface brightness streams is tricky, but it will be crucial if we want to use the many future stream detections (e.g., from Roman, Rubin, and Euclid) for dark matter science. In this work, we have used the radial velocity estimate from the nuclear star cluster in Dw3 (Dumont et al. 2022). But often we do not detect the progenitors of extragalactic streams (see, e.g., Martinez-Delgado et al. 2021) and can only observe the diffuse light in the actual streams.

Even without a known progenitor, like the Dw3 nuclear star cluster used in this work, GCs provide bright signposts that can be used to determine stream velocities. Significant GC populations are found associated with MW streams (e.g., Malhan et al. 2022), in addition to those in M31 (Veljanoski et al. 2014). With the caveat of not always knowing the line-of-sight distance and thereby the true association of the GCs with the streams, velocities of GCs can be measured with current instrumentation out to distances of ~30 Mpc (Brodie et al. 2014). Future extremely large telescopes will extend this distance limit by about a factor of three, potentially enabling halo mass determinations in a wide range of halo masses and environments with the method presented in this paper.

If the streams do not host GCs, the radial velocities along the streams can also be estimated from the technique presented in Toloba et al. (2016a). In particular, they study the internal stellar kinematics of low surface brightness streams beyond the Local Group. Their technique relies on multi-object spectroscopy of individual stars using the DEIMOS spectrograph (Faber et al. 2003) on Keck (see also Guhathakurta et al. 2006, for DEIMOS spectra of individual stars in the Giant Southern Stream of M31), although similar science can be done with any large ground-based telescope with wide-field multi-object spectroscopy capabilities. They place slitlets on the brightest available stars in the stream, including the tip of the red-giant branch and asymptotic-giant branch stars, along with stellar blends. By using traditional spectral stacking techniques (see Section 2 of Toloba et al. 2016a, for a detailed description), sufficient signal-to-noise is built up to measure bulk kinematic properties. Toloba et al. (2016a) apply their method to the stream around the NGC 4449 dwarf galaxy, which is at a distance of 3.82 Mpc (Martínez-Delgado et al. 2012), and they find a flat velocity gradient along the NGC 4449 stream with a typical error of 10-20 km s⁻¹. See also the work of Toloba et al. (2016b), who used this method to determine the velocity and metallicity of an M81 satellite dwarf galaxy. Cen A is at a distance similar to that of NGC 4449, and we expect similar errors for any future radial velocity measurements along the Dw3 stream with this method. Based on Figure 9, we note that, while this will only allow us to, at best, distinguish between the most extreme cases of viable dark matter halos, even just the sign of the radial velocity gradient along the stream will be informative.

While DEIMOS can only be used out to ∼5 Mpc in the northern sky (Toloba et al. 2016b), it is possible that the Very Large Telescope's (VLT's) IFU can be used for similar purposes. ESO's Extremely Large Telescope (ELT; planned to receive first light in 2027) will be suitable for the Toloba et al. (2016a) method, and could potentially target faint surface

brightness features, such as streams, out to distances 2–3 times farther than the VLT (e.g., the Virgo Cluster at $d \sim 16.5$ Mpc).

While we might not be able to obtain radial velocities along all future observations of extragalactic streams, even with the ELT or GCs, these streams can still inform accretion histories, and their number counts and surface brightnesses will provide crucial comparisons to Λ CDM (e.g., T. Starkenburg et al. 2022, in preparation).

6. Conclusion

In this paper, we have explored whether the straight stream emerging from Dw3 could be reproduced in the halo of the elliptical galaxy Cen A, and what constraining power the stream holds on Cen A's dark matter halo mass. We have used simple stream models and a new external galaxy stream-fitting technique to explore large grids of orbital parameters. We combined our method with a Jacobi radius cut to ensure realistic tidal stripping. We conclude the following:

- 1. To reproduce the straight nature of the Dw3 stream at a projected distance of 79 kpc in Cen A's halo, we find that only a small pocket of orbital solutions for the Dw3 progenitor yield good fits to the data. These solutions all require that Dw3 moves very rapidly in the direction parallel to the stream and slowly in the direction perpendicular to the stream.
- 2. If we only have observations of the morphology and track of a stream, it is not possible to constrain the dark matter halo, because the orbital velocity of the stream, as well as the progenitor mass and integration time, can be scaled to produce the exact same morphology in an arbitrary halo mass.
- 3. If we include observations of just one radial velocity, we can constrain the halo mass of Cen A. When we fix the observed distances to Cen A and Dw3, the Dw3 stream can only reproduce the control data for a minimum Cen A halo mass of $M_{200} > 4.70 \times 10^{12} M_{\odot}$. This is consistent with studies of Cen A's GC and dwarf galaxy kinematics.
- 4. We test the best-fit model stream's morphology with an *N*-body simulation including a Dw3 dark matter component, and confirm that we obtain the same stream morphology with more realistic tidal stripping conditions.
- 5. The radial velocity and distance gradients along the Dw3 stream can help constrain the halo mass of Cen A further. In particular, the end points of the stream are most informative, because they display the largest difference for different halo masses.
- 6. If the line-of-sight distance to Dw3 is greater than the line-of-sight distance to Cen A, our models predict that the southern parts of the Dw3 stream are more blueshifted than the northern parts. The sign of the radial velocity gradient along the stream can help distinguish between whether Dw3 is located in front of or behind Cen A.
- 7. The second stream in Cen A's halo can easily be reproduced in the fiducial halo of Cen A as well as in the lowest-mass halo included in this work.

We stress that extragalactic stellar streams provide a fundamental way of mapping the dark matter in our universe, which is otherwise only possible through lensing studies, GC kinematics, integrated light velocity dispersions, and rotation curves of galaxies. Given the streams' potential to generate discoveries about dark matter, we urge the extragalactic stream

community to focus their efforts on radial velocity follow-up plans.

We thank the CCA Dynamics Group, E. Tollerud, A. Bonaca, A. Dumont, J. Strader, and T. Starkenburg for insightful discussions. We also thank J. Strader and A. K. Hughes for providing Centaurus A globular cluster data and analysis. Support for this work was provided by NASA through the NASA Hubble Fellowship grant #HST-HF2-51466.001-A awarded by the Space Telescope Science Institute, which is operated by the Association of Universities for Research in Astronomy, Incorporated, under NASA contract NAS5-26555. The Flatiron Institute is supported by the Simons Foundation. D.J.S. acknowledges support from NSF grants AST-1821967 and 1813708. Research by D.C. is supported by NSF grant AST-1814208.

Software: Astropy (Astropy Collaboration et al. 2013, 2018), Matplotlib (Hunter 2007), Gala (Price-Whelan 2017; Price-Whelan et al. 2020), Numpy (Harris et al. 2020), Scipy (Virtanen et al. 2020).

ORCID iDs

Sarah Pearson https://orcid.org/0000-0003-0256-5446 Adrian M. Price-Whelan https://orcid.org/0000-0003-0872-7098

David W. Hogg https://orcid.org/0000-0003-2866-9403
Anil C. Seth https://orcid.org/0000-0003-0248-5470
David J. Sand https://orcid.org/0000-0003-4102-380X
Jason A. S. Hunt https://orcid.org/0000-0001-8917-1532
Denija Crnojević https://orcid.org/0000-0002-1763-4128

References

Astropy Collaboration, Price-Whelan, A. M., Sipőcz, B. M., et al. 2018, AJ, 156, 123

Astropy Collaboration, Robitaille, T. P., Tollerud, E. J., et al. 2013, A&A, 558, A33

Behroozi, P. S., Conroy, C., & Wechsler, R. H. 2010, ApJ, 717, 379
Belokurov, V., Zucker, D. B., Evans, N. W., et al. 2006, ApJL, 642, L137

Bonaca, A., & Hogg, D. W. 2018, ApJ, 867, 101 Bovy, J., Bahmanyar, A., Fritz, T. K., & Kallivayalil, N. 2016, ApJ, 833, 31 Bressan, A., Marigo, P., Girardi, L., et al. 2012, MNRAS, 427, 127

Brodie, J. P., Romanowsky, A. J., Strader, J., et al. 2012, MNRAS, 421, 127

Carlin, J. L., Garling, C. T., Peter, A. H. G., et al. 2019, ApJ, 886, 109 Crnojević, D., Sand, D. J., Bennet, P., et al. 2019, ApJ, 872, 80

Crnojević, D., Sand, D. J., Spekkens, K., et al. 2016, ApJ, 823, 19

Dillamore, A. M., Belokurov, V., Evans, N. W., & Price-Whelan, A. M. 2022, MNRAS, 516, 1685

Dumont, A., Seth, A. C., Strader, J., et al. 2022, ApJ, 929, 147

Frkal D. Konosov S. E. & Belokurov V. 2017, MNRAS, 470

Erkal, D., Koposov, S. E., & Belokurov, V. 2017, MNRAS, 470, 60 Fabbiano, G., Kim, D. W., & Trinchieri, G. 1992, ApJS, 80, 531

Faber, S. M., Phillips, A. C., Kibrick, R. I., et al. 2003, Proc. SPIE, 4841, 1657
Fardal, M., Guhathakurta, P., Gilbert, K., et al. 2009, in ASP Conf. Ser. 419,
Galaxy Evolution: Emerging Insights and Future Challenges, ed. S. Jogee

et al. (San Francisco, CA: ASP), 118
Fardal, M. A., Guhathakurta, P., Babul, A., & McConnachie, A. W. 2007,

Fardal, M. A., Huang, S., & Weinberg, M. D. 2015, MNRAS, 452, 301
Fardal, M. A., Weinberg, M. D., Babul, A., et al. 2013, MNRAS, 434, 2779

Fritz, T. K., & Kallivayalil, N. 2015, ApJ, 811, 123 Garavito-Camargo, N., Besla, G., Laporte, C. F. P., et al. 2019, ApJ, 884, 51 Gibbons, S. L. J., Belokurov, V., & Evans, N. W. 2014, MNRAS, 445, 3788 Gilbert, K. M., Guhathakurta, P., Kollipara, P., et al. 2009, ApJ, 705, 1275

Graham, J. A. 1979, ApJ, 232, 60 Guhathakurta, P., Rich, R. M., Reitzel, D. B., et al. 2006, AJ, 131, 2497

Guhathakurta, P., Rich, R. M., Reitzel, D. B., et al. 2006, AJ, 131, 2497 Harris, C. R., Millman, K. J., van der Walt, S. J., et al. 2020, Natur, 585, 357 Harris, G. L. H., Harris, W. E., & Poole, G. B. 1999, AJ, 117, 855

```
Harris, G. L. H., Rejkuba, M., & Harris, W. E. 2010, PASA, 27, 457
Hendel, D., Johnston, K. V., Patra, R. K., & Sen, B. 2019, MNRAS, 486, 3604
Hernquist, L. 1990, ApJ, 356, 359
```

Hughes, A. K., et al. 2022, arXiv:2208.08997

Hughes, A. K., Sand, D. J., Seth, A., et al. 2021, ApJ, 914, 16

Hui, X., Ford, H. C., Freeman, K. C., & Dopita, M. A. 1995, ApJ, 449, 592 Hunter, J. D. 2007, CSE, 9, 90

Ibata, R., Chapman, S., Ferguson, A. M. N., et al. 2004, MNRAS, 351, 117 Ivezic, Z., Axelrod, T., Brandt, W. N., et al. 2008, SerAJ, 176, 1

Ivezic, Z., Axelrod, T., Brandt, W. N., et al. 2008, SerAJ, 176, 1 Jarrett, T. H., Chester, T., Cutri, R., Schneider, S. E., & Huchra, J. P. 2003, AJ,

Johnston, K. V., Sackett, P. D., & Bullock, J. S. 2001, ApJ, 557, 137Johnston, K. V., Spergel, D. N., & Hernquist, L. 1995, ApJ, 451, 598

Kado-Fong, E., Greene, J. E., Greco, J. P., et al. 2020, AJ, 159, 103

Kado-Fong, E., Greene, J. E., Hendel, D., et al. 2018, ApJ, 866, 103

Karachentsev, I. D., Sharina, M. E., Dolphin, A. E., et al. 2002, A&A, 385, 21

Kawata, D., & Gibson, B. K. 2003, MNRAS, 340, 908

Koposov, S. E., Rix, H.-W., & Hogg, D. W. 2010, ApJ, 712, 260 Küpper, A. H. W., Balbinot, E., Bonaca, A., et al. 2015, ApJ, 803, 80

Laine, S., Martinez-Delgado, D., Trujillo, I., et al. 2018, arXiv:1812.04897

Laureijs, R., Amiaux, J., Arduini, S., et al. 2011, arXiv:1110.3193 Law, D. R., & Majewski, S. R. 2010, ApJ, 718, 1128

Li, T. S., Koposov, S. E., Zucker, D. B., et al. 2019, MNRAS, 490, 3508

Li, T. S., Ji, A. P., Pace, A. B., et al. 2022, ApJ, 928, 30 Lilleengen, S., Petersen, M. S., Erkal, D., et al. 2022, MNRAS, 518, 774

Malhan, K., Ibata, R. A., Sharma, S., et al. 2022, ApJ, 926, 107 Martin, N. F., Ibata, R. A., Rich, R. M., et al. 2014, ApJ, 787, 19

Martin, N. F., Ibata, R. A., Rich, R. M., et al. 2014, ApJ, 767, 19

Martínez-Delgado, D., Romanowsky, A. J., Gabany, R. J., et al. 2012, ApJL, 748, L.24

Martinez-Delgado, D., Cooper, A. P., Roman, J., et al. 2021, arXiv:2104.06071 McConnachie, A. W., Irwin, M. J., Ibata, R. A., et al. 2009, Natur, 461, 66

McConnachie, A. W., Ibata, R., Martin, N., et al. 2018, ApJ, 868, 55 McLeod, B., Geary, J., Conroy, M., et al. 2015, PASP, 127, 366

Muñoz-Cuartas, J. C., Macciò, A. V., Gottlöber, S., & Dutton, A. A. 2011, MNRAS, 411, 584

Müller, O., Lelli, F., Famaey, B., et al. 2022, A&A, 662, A57

Müller, O., Pawlowski, M. S., Jerjen, H., & Lelli, F. 2018, Sci, 359, 534

Müller, O., Pawlowski, M. S., Lelli, F., et al. 2021, A&A, 645, L5

Naidu, R. P., Conroy, C., Bonaca, A., et al. 2020, ApJ, 901, 48

Navarro, J. F., Frenk, C. S., & White, S. D. M. 1996, ApJ, 462, 563
Nibauer, J., Belokurov, V., Cranmer, M., Goodman, J., & Ho, S. 2022, ApJ, 940, 22

Pearson, S., & Clark, S. E. 2021, HSS: The Hough Stream Spotter, Astrophysics Source Code Library, ascl:2109.014

Pearson, S., Clark, S. E., Demirjian, A. J., et al. 2022, ApJ, 926, 166 Pearson, S., Küpper, A. H. W., Johnston, K. V., & Price-Whelan, A. M. 2015,

ApJ, 799, 28 Peng, E. W., Ford, H. C., & Freeman, K. C. 2004, ApJ, 602, 685 Plummer, H. C. 1911, MNRAS, 71, 460

Price-Whelan, A., Sipocz, B., Lenz, D., et al. 2020, adrn/gala: v1.3, Zenodo, doi:10.5281/zenodo.4159870

Price-Whelan, A. M. 2017, JOSS, 2, 388

Price-Whelan, A. M., & Bonaca, A. 2018, ApJL, 863, L20

Price-Whelan, A. M., Johnston, K. V., Valluri, M., et al. 2016, MNRAS, 455, 1079

Shang, Z., Zheng, Z., Brinks, E., et al. 1998, ApJL, 504, L23

Shipp, N., Erkal, D., Drlica-Wagner, A., et al. 2021, ApJ, 923, 149

Shipp, N., Li, T. S., Pace, A. B., et al. 2019, ApJ, 885, 3

Silge, J. D., Gebhardt, K., Bergmann, M., & Richstone, D. 2005, AJ, 130, 406 Spergel, D., Gehrels, N., Breckinridge, J., et al. 2013, arXiv:1305.5422

Toloba, E., Guhathakurta, P., Romanowsky, A. J., et al. 2016a, ApJ, 824, 35

Toloba, E., Sand, D., Guhathakurta, P., et al. 2016b, ApJL, 830, L21 van Dokkum, P., Gilhuly, C., Bonaca, A., et al. 2019, ApJL, 883, L32

Veljanoski, J., Mackey, A. D., Ferguson, A. M. N., et al. 2014, MNRAS, 442, 2929

Vera-Ciro, C., & Helmi, A. 2013, ApJL, 773, L4

Virtanen, P., Gommers, R., Oliphant, T. E., et al. 2020, NatMe, 17, 261

Wang, J., Hammer, F., Rejkuba, M., Crnojević, D., & Yang, Y. 2020, MNRAS, 498, 2766

Woodley, K. A., Gómez, M., Harris, W. E., Geisler, D., & Harris, G. L. H. 2010, AJ, 139, 1871

Woodley, K. A., Harris, W. E., Beasley, M. A., et al. 2007, AJ, 134, 494
Yavetz, T. D., Johnston, K. V., Pearson, S., Price-Whelan, A. M., & Weinberg, M. D. 2021, MNRAS, 501, 1791